Quantitative evaluation of polarimetric estimates from scanning weather radars using a vertically pointing micro rain radar

Reinoso-Rondinel, Ricardo; Schleiss, Marc

DOI
10.1175/JTECH-D-20-0062.1

Publication date
2021

Document Version
Final published version

Published in
Journal of Atmospheric and Oceanic Technology

Citation (APA)
Reinoso-Rondinel, R., & Schleiss, M. (2021). Quantitative evaluation of polarimetric estimates from scanning weather radars using a vertically pointing micro rain radar. *Journal of Atmospheric and Oceanic Technology*, *38*(3), 481-499. https://doi.org/10.1175/JTECH-D-20-0062.1

Quantitative Evaluation of Polarimetric Estimates from Scanning Weather Radars Using a Vertically Pointing Micro Rain Radar

RICARDO REINOSO-RONDINEL[a,b] AND MARC SCHLEISS[a]

[a] *Department of Geosciences and Remote Sensing, Faculty of Civil Engineering and Geosciences, Delft University of Technology, Delft, Netherlands*

(Manuscript received 25 April 2020, in final form 28 November 2020)

ABSTRACT: Conventionally, Micro Rain Radars (MRRs) have been used as a tool to calibrate reflectivity from weather radars, estimate the relation between rainfall rate and reflectivity, and study microphysical processes in precipitation. However, limited attention has been given to the reliability of the retrieved drop size distributions (DSDs) from MRRs. This study sheds more light on this aspect by examining the sensitivity of retrieved DSDs to the assumptions made to map Doppler spectra into size distributions, and investigates the capability of an MRR to assess polarimetric observations from operational weather radars. For that, an MRR was installed near the Cabauw observatory in the Netherlands, between the International Research Center for Telecommunications and Radar (IRCTR) Drizzle Radar (IDRA) X-band radar and the Herwijnen operational C-band radar. The measurements of the MRR from November 2018 to February 2019 were used to retrieve DSDs and simulate horizontal reflectivity Z_e, differential reflectivity Z_{DR}, and specific differential phase K_{DP} in rain. Attention is given to the impact of aliased spectra and right-hand-side truncation on the simulation of polarimetric variables. From a quantitative assessment, the correlations of Z_e and Z_{DR} between the MRR and Herwijnen radar were 0.93 and 0.70, respectively, while those between the MRR and IDRA were 0.91 and 0.69. However, Z_e and Z_{DR} from the Herwijnen radar showed slight biases of 1.07 and 0.25 dB. For IDRA, the corresponding biases were 2.67 and −0.93 dB. Our results show that MRR measurements are advantageous to inspect the calibration of scanning radars and validate polarimetric estimates in rain, provided that the DSDs are correctly retrieved and controlled for quality assurance.

KEYWORDS: Data processing; Data quality control; Measurements; Radars/Radar observations; Weather radar signal processing

1. Introduction

Micro Rain Radars (MRRs) are small portable vertical profilers that can be used to calibrate reflectivity from weather radars, improve the relation between reflectivity factor (Z) and rainfall rate (R), and study microphysical processes in precipitation (e.g., Wingo et al. 2018; Chen et al. 2015). This is possible thanks to the MRR's capability of estimating vertical profiles of particle size distributions from Doppler spectra profiles, from which bulk quantities such as rainfall rate and liquid water content can be obtained. The theoretical basis for retrieving drop size distributions (DSDs) is the relationship between the terminal fall velocity of a raindrop and its diameter, as explained in Sekhon and Srivastava (1971) and Atlas et al. (1973). However, this relation is sensitive to vertical air velocity, which can affect the accuracy of retrieved DSDs (Peters et al. 2010). For example, Tridon et al. (2011) analyzed the impact of Doppler aliasing due to vertical wind on Z and R estimates and suggested an automatic way to identify and remove DSDs corrupted by aliasing. Adirosi et al. (2016) used a 2D video disdrometer (2DVD) to correct MRR-based DSDs at 105 m for the effects of vertical winds in heavy rain conditions. Richter and Hagen (1997) presented an experimental setup in Germany to retrieve DSD parameters from an L-band vertical pointing radar that is able to separate the air velocity from the raindrop velocity, a dual-polarization C-band radar, and a disdrometer.

Given the potential of using MRRs to study the variability of the Z–R relation, multiple researchers have tried to assess the accuracy of rainfall rate, taking into account rain type and microphysics. Peters et al. (2005) analyzed 5 years of MRR data below the melting layer to study the vertical variability of MRR-based DSD profiles and its impact on the Z–R relation. This work suggested that in light rain, R values resulting from conventional Z–R relations agree the MRR-based R values whereas in heavy precipitation, with rainfall rates larger than 20 mm h^{-1}, the Z–R relations tend to underestimate R due to vertical variability of the DSD and attenuation. They also presented an attenuation correction scheme, which was later extended by Peters et al. (2010). Kumar et al. (2017) investigated DSDs during the Indian summer monsoon using a MRR and a disdrometer in order to adapt the Z–R relation to precipitation type and rain microphysics. van Baelen et al. (2009) suggested several Z–R relations for different precipitation regimes using observations from an MRR and an X-band radar. Kowalewsky and Peters (2010) studied the impact of the linear depolarization ratio (L_{DR}) retrieved from a cloud radar within the melting layer on MRR-based DSDs in order to improve the Z–R relation. Mazari et al. (2017) used an MRR to study the vertical variability of rain and quantify the accuracy of the Z–R relation from an S-band radar.

Frech et al. (2017) conducted research on the absolute calibration of a dual-polarization C-band radar using an MRR to

[b] Current affiliation: Department of Meteorology, Institute for Geosciences, University of Bonn, Bonn, Germany.

Corresponding author: Ricardo Reinoso-Rondinel, ricardoreinoso232@gmail.com

DOI: 10.1175/JTECH-D-20-0062.1

verify whether a disdrometer can represent radar measurements 650 m above the height of a C-band radar. They found that the vertical variability of reflectivity in the 650 m column is small only for warm stratiform events characterized by raindrop fall velocities smaller than 2 m s^{-1} and reflectivity in the range of 15–35 dBZ. Adirosi et al. (2020) also performed a calibration study of a dual-polarization S-band radar by simulating reflectivity and differential reflectivity vertical profiles from MRR DSD and T-matrix simulation. Their study showed a good agreement in terms of reflectivity between the S-band radar and the MRR with an absolute bias of 3 dB; whereas for differential reflectivity, the dispersion was larger. Lengfeld et al. (2016, 2018) compared reflectivity attenuation correction methods from a network of single polarization X-band radars, including a network of MRRs for validation purposes in different precipitation types (i.e., stratiform, convective, and mixed). It was shown that the methods that consider measurements from C- or S-band radars lead to the best attenuation correction results quantified by a correlation coefficient of 0.88 and a bias of −0.03 dB resulting from the X-band and the MRR radar network. To evaluate the methods, the X-band radars at an elevation angle of 3° were calibrated using measurements from the MRR at the corresponding height.

So far, however, research has mostly focused on analyzing relations among DSD parameters as well as the Z–R relation while limited attention has been given to the possibility of using retrieved DSDs to study polarimetric radar variables. In this work, the following points are therefore examined: 1) the sensitivity of the retrieved DSDs to the assumptions made to map profiles of Doppler spectra into profiles of DSD (e.g., the minimum and maximum drop diameter, temperature, and spectra aliasing), 2) the impact of distinct radar resolution volumes on simultaneous observations from scanning radars and the MRR, and 3) the possibility to use an MRR to verify polarimetric variables estimated by operational radars. The approach can be summarized as follows: retrieved DSD profiles from MRR measurements are used to simulate profiles of polarimetric variables such as equivalent horizontal reflectivity (Z_e), differential reflectivity (Z_{DR}), and specific differential phase (K_{DP}). The simulated estimates are then used to evaluate the accuracy and consistency of Z_e, Z_{DR}, and K_{DP} that are obtained from scanning radars, taking into account their sensitivity to the maximum drop diameter, distinct radar resolution volume, and precipitation type.

This paper is organized as follows. Section 2 introduces the experimental setup and the radar specifications while section 3 describes the methods for selecting events, retrieving DSDs, processing the data from the two dual-polarimetric scanning radars, and comparing the different polarimetric variables. Section 4 analyzes the consistency of polarimetric variables between those simulated by the MRR and those measured by two scanning radars. In addition, it assesses the bias on Z_e and Z_{DR} measured by the scanning radars. Section 5 draws the conclusions.

2. Experimental setup and data

a. Experimental setup

The setup consists of three radar systems, two of which are scanning radars at X-band and C-band frequencies while the third one is a vertically pointing MRR at K-band frequencies. These radars are located in the vicinity of the Cabauw Experimental Site for Atmospheric Research (CESAR) observatory in the Netherlands (NL) (Leijnse et al. 2010). The X-band and C-band radar will be referred to as the International Research Center for Telecommunications and Radar (IRCTR) Drizzle Radar (IDRA) and Herwijnen radar, respectively. The locations of these radars are shown in Fig. 1. IDRA is located at the CESAR observatory at the top of a flux tower at a height of 213 m above ground level. The MRR is on the camping site ''De Victorie'' in the town of Meerkerk, 4.65 km from IDRA, and is collocated with a Davis Vantage Pro weather station. The height of the MRR antenna is 1.5 m above ground and it is free of any obstacles along the radar beam. The Herwijnen radar is placed on top of a 22 m tower located 20.8 km southeast from IDRA and 16.2 km from the MRR. It is part of the current operational network of polarimetric C-band weather radars in the Netherlands.

This unique setup means that collocated observations of precipitation from independent radar systems operating at different frequencies and range resolutions can be compared. The MRR is close enough from the IDRA and Herwijnen radars to limit attenuation levels that accumulate at long ranges yet far enough from both radars to avoid near-range antenna effects and ground clutter. The height at which the IDRA and the Herwijnen radar beams overlap (~150–350 m) is low enough to be below the common height of the melting layer (~1–3 km). Moreover, the broadening of the IDRA and Herwijnen radar beams at the range of the MRR is small, with corresponding azimuthal resolutions in the order of 200–300 m, making the setup very suitable in terms of volume matching. The terrain around the setup is mostly rural and flat, with the ground level varying only within ±1 m.

For the purpose of obtaining collocated radar measurements, it is important to estimate the resolution volumes resulting from the three radars. Figure 2 shows the corresponding radar volumes, centered along the vertical MRR beam. For simplicity, the shape of the radar volumes is assumed cylindrical. The dimensions of the sampling volumes are estimated based on the distance to the radar, the beamwidth, the range resolution, the height of the radar, and the elevation angle. The vertical positions of the IDRA and Herwijnen radar volumes correspond to elevation (azimuthal) angles of 0.5° (144.8°) and 0.8° (313°), respectively. Note that, in the vertical direction, 8 MRR range gates are needed to intercept that of Herwijnen, while 6 range gates are required for IDRA. Moreover, the resolution volume of the Herwijnen radar is ~14 times that of IDRA while the one from IDRA is ~660 times that of the MRR. The resolution volume of the Herwijnen radar is therefore ~10^3 times that of the MRR.

b. Data sources and technical specifications

1) MRR

The vertical pointing K-band radar, also referred to as the MRR, measures time series of vertical profiles of precipitation, therefore providing insight into the temporal evolution of a

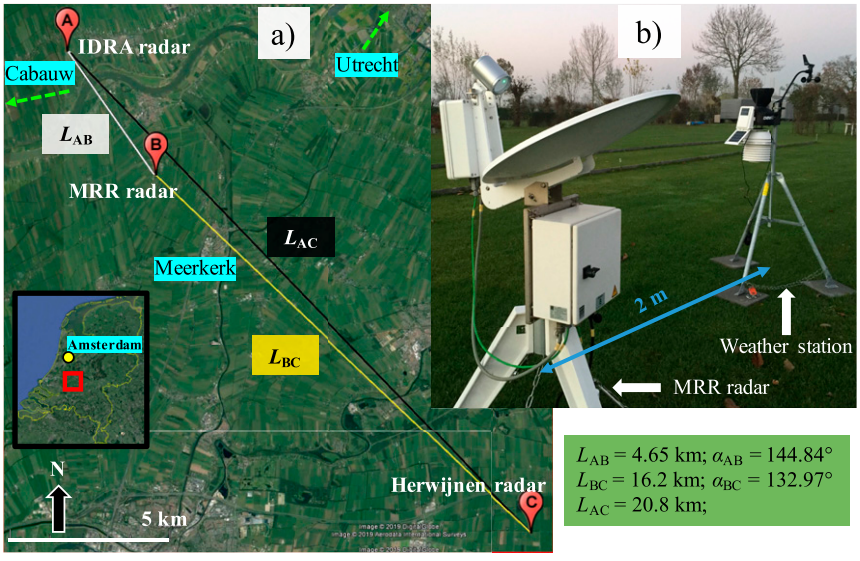

FIG. 1. Radar network representation. (a) The location of the three radars are indicated by the points: A–IDRA; B—MRR; and C—Herwijnen. The labels L_{AB}, L_{BC}, and L_{AC} illustrate the distance between the pairs A–B, B–C, and A–C, respectively. The values of these labels are shown in the green box along with the angles between A–B and B–C, using the north as the 0° reference. The village of Cabauw and the city of Utrecht are located 2 km west and 19 km northeast from IDRA, respectively. The red square inside the map of the Netherlands indicates the location of the study area with respect to the city of Amsterdam. (b) A photograph that displays the MRR radar and the weather station, both installed in the camping site De Victorie in Meerkerk.

weather system along the vertical dimension from the perspective of a fixed observer on the ground. The MRR provides estimates of, among others, spectral reflectivity η (m^{-1}), equivalent reflectivity Z_e (dBZ), mean radial Doppler velocity v_r ($m\,s^{-1}$), path-integrated attenuation (PIA) (dB), rainfall rate R ($mm\,h^{-1}$), and melting-layer detection. The instrument used in this study is the new state of the art MRR-PRO model (see Table 1 for specifications) manufactured by METEK in Germany with a sampling rate f_s of 500 kHz, which is 4 times faster than the previous model, the MRR2 (METEK 2015). The user interface makes it possible to configure the MRR for various operational purposes. In this experiment, the number of spectra components n_s, the number of range gates n_g, and the range resolution Δr_M were set to 64, 128, and 35 m, respectively. This leads to a resolution in the spectral domain of $\Delta f = f_s/(2n_sn_g)$ equal to 30.52 Hz. At the time of the experiment, the MRR included a software bug that prevented the storage of retrieved DSD profiles. The DSDs therefore had to be retrieved from the recorded spectral reflectivity profiles as explained in section 3c instead of being directly available through the software.

2) HERWIJNEN AND IDRA RADARS

The Royal Netherlands Meteorological Institute (Koninklijk Nederlands Meteorologisch Instituut) (KNMI) operates a network of two C-band radars supplied by Selex ES with dual-polarization capabilities, installed in Herwijnen and Den Helder. Each radar covers a volumetric region every 5 min by rotating the antenna 360° in azimuth and tilting the antenna in elevation from 0.3° to 25°. Additionally, the radars perform a bird-bath scan for calibration purposes of differential reflectivity every 5 min. The calibration of reflectivity is performed using an extended version of the sun-signal method (Rinehart 2004; Leijnse et al. 2010). Besides reflectivity and differential reflectivity, polarimetric variables include differential phase, specific differential phase, and cross-polar correlation coefficient. Table 1 summarizes the configuration of the Herwijnen radar at the elevation angle of 0.8° with a range resolution of 225 m. (The data are freely available at https://data.knmi.nl/datasets under the open data policy of the Dutch government.)

The fully polarimetric X-band weather radar IDRA (Figueras i Ventura 2009) is a horizontally scanning research radar designed and operated by the Delft University of Technology and its technical specifications are given in Table 1. The operational range and range resolution are equal to 15.3 km and 30 m, respectively. The antenna rotates over 360° in 1 min at a fixed elevation angle of 0.5° due to mechanical limitations. Clutter echoes are removed by a filter based on spectral polarimetric processing (Unal 2009). Measurements obtained by IDRA include reflectivity, differential reflectivity, and differential phase. Because these measurements have high spatial and temporal resolution of 30 m and 1 min, IDRA reduces the sampling gap between the Herwijnen (225 m and 5 min) and MRR radar (35 m and 10 s), offering the possibility to study the effect of spatial and temporal resolutions on the accuracy and consistency of the measurements. In addition, the polarimetric capability of IDRA

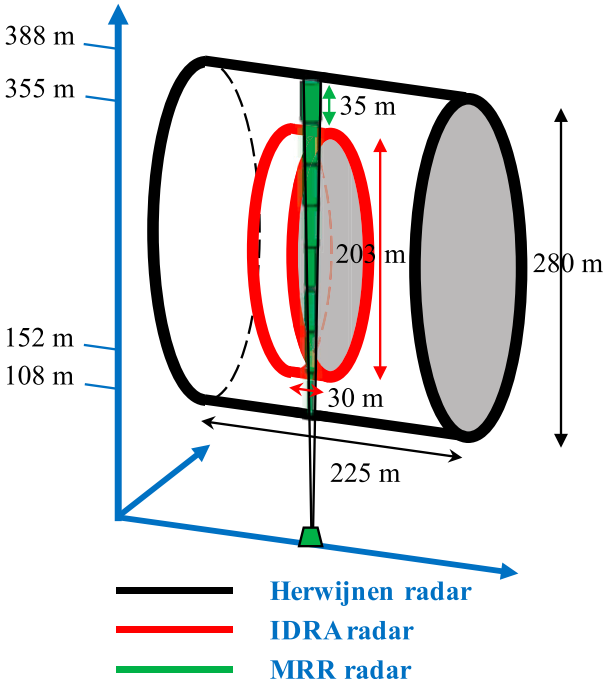

FIG. 2. Schematic representation of radars' resolution volumes. The green trapezoid indicates the MRR while the green cylinders represent the resolution volumes in height, which are collocated with the resolution volume of the IDRA radar (red) and the Herwijnen radar (black) at elevation angles of 0.5° and 0.8°, respectively.

allows direct measurements of the linear depolarization ratio L_{DR} (dB), which is helpful for filtering out range gates with low signal-to-noise ratio (SNR) (dB) and better distinguishing rain from other hydrometeors. Note that in this work, "a low SNR" is used as a qualitative label rather than a quantitative attribute to refer to areas in which a radar system can hardly distinguish the weather signal from the system noise level. (The data collected by IDRA are freely available in the atmospheric sciences repository at https://opendap.tudelft.nl/thredds/catalog/IDRA/catalog.html; Otto et al. 2010.)

3) WEATHER STATION

A Davis Instrument weather station was collocated with the MRR with the purpose of monitoring atmospheric conditions such as temperature and wind velocity in the vicinity of the MRR, as well as rainfall amounts, helping with the interpretation and quality control of the radar data. The weather station is controlled by the Vantage Pro2 console that is connected to a local laptop with the serial datalogger 6510SER model. The console and laptop were installed in a storage shed ~10 m from the weather station. For this experiment, the sampling resolution was set to 5 min. The tipping bucket in the rain collector is calibrated such that the bucket is tipped at steps of 0.20 mm and rainfall rate is calculated based on the time interval between each tip. The relatively large volume of the tipping-bucket rain gauge is not optimal for measuring low rainfall intensities at high temporal resolutions. However, this is not critical as the main purpose of the rain gauge is not to provide detailed information about the rainfall rate, but to provide a rough, independent estimate of the total accumulated rainfall amount for each event to be used for quality control purposes. The weather station also records estimates of average wind speed and dominant direction using an anemometer. The temperature sensor is vented and shielded, and it records measurements every 5 min. For more details on the weather station, the reader is referred to the Vantage Pro2 console manual (https://www.davisinstruments.com/product_documents/weather/manuals/07395-234_IM_06312.pdf).

TABLE 1. Technical specifications for the three radars. The specifications for the Herwijnen radar correspond to the elevation angle of 0.8°.

Parameter	MRR	IDRA	Herwijnen
Radar type	FMCW	FMCW	Pulsed
Polarization	Single	Full	Dual
Frequency	24.15 GHz	9.475 GHz	5.6 GHz
Range resolution	35 m	30 m	225 m
Max range	4.5 km	15.3 km	187.3 km
Max velocity	12.3 m s^{-1}	19 m s^{-1}	24 m s^{-1}
Velocity resolution	0.1905 m s^{-1}	0.03 m s^{-1}	0.189 m s^{-1}
Revisit time	10 s	1 min	5 min
Beamwidth	2°	1.8°	1°
Height	0 m	213 m	22 m

3. Methods

In this section, the steps to retrieve DSDs from spectra reflectivity measured by the MRR and further steps to quality control the accuracy of DSDs are described. Also, the main processing steps applied to the Herwijnen and IDRA data are listed. Finally, the method used to simulate polarimetric radar variables from retrieved DSDs, as if they were observed by the Herwijnen and IDRA radar, is explained.

a. *Description of selected events*

The measurement period November 2018–February 2019 contains 15 major rain events (E1–E15) described in Table 2. The rain accumulation and maximum values of rainfall rate, wind speed, wind direction, and temperature are obtained from the weather station. Rainfall rates are classified as light, moderate or heavy according to their maximum rainfall intensity (R_{max}), using the thresholds suggested by the American Meteorological Society (2019). Light rain is defined as $R_{max} \leq 2.5$ mm h^{-1}, moderate rain as $2.5 < R_{max} \leq 7.6$ mm h^{-1}, and heavy rain as $R_{max} > 7.6$ mm h^{-1}. It can be seen that most of the events were characterized by rain accumulations of less than 10 mm, while only events E14 and E15 reached rain accumulation values of 14 and 17.4 mm, respectively. A peak value of R_{max} equal to 12.2 mm h^{-1} was found in E4 and E8 and the largest maximum wind speed of 14.7 m s^{-1} was registered in E5. The maximum and minimum temperatures were in the range of 2°–11°C and 0°–8°C, respectively.

Figures 3a–d illustrates the observations for event E4 from the viewpoints of the three radars. While the MRR captures

TABLE 2. Description of the 15 rainfall events in 2018–19 considered for the analyses. The labels R_{max}, W^s_{max}, W^d_{max}, and T_{max} indicate the maximum rainfall rate, wind speed, wind direction, and temperature obtained from the weather station data. The lines in boldface represent events with a low height of the melting layer seen from the MRR data.

Event	Date	Duration (UTC)	Type	Accumulation (mm)	R_{max} (mm h^{-1})	W^s_{max} (m s^{-1})	W^d_{max}	T_{max} (°C)
E1	11 Nov	0400–0800	Heavy	8.8	9.1	5.3	SE	11.2
E2	12 Nov	0500–1300	Moderate	6.7	3.0	2.7	SE	11.5
E3	2 Dec	0300–0700	Moderate	5.6	6.1	6.2	SE	10.3
E4	7 Dec	0300–1700	Heavy	11.8	12.2	11.1	ESE	11.7
E5	8 Dec	0600–2300	Heavy	11.1	9.1	14.7	SSE	10.8
E6	9 Dec	0400–2300	Heavy	7.3	9.1	12.5	S	9.2
E7	21 Dec	0300–0900	Moderate	11.1	6.1	8.0	SE	9.7
E8	22 Dec	0100–0400	Heavy	7.3	12.2	8.9	SSE	9.3
E9	23 Dec	0900–2300	Moderate	10.5	6.1	5.8	WNW	8.1
E10	**17 Jan**	**1700–2100**	**Moderate**	**0.5**	**3.0**	**8.0**	**SW**	**2.1**
E11	26 Jan	2200–0000	Moderate	3.5	3.0	9.4	E	6.8
E12	27 Jan	0100–1300	Moderate	6.3	6.1	8.9	SW	7.2
E13	**28 Jan**	**0000–1000**	**Moderate**	**3.3**	**6.1**	**11.1**	**WSW**	**4.8**
E14	6 Feb	0600–2200	Moderate	14.0	6.1	6.7	SE	6.7
E15	10 Feb	0200–1400	Moderate	17.4	6.1	9.8	SSE	9.2

the vertical structure of precipitation over time, the IDRA and Herwijnen radar capture the horizontal structure and evolution of the event. Note that when the convective region passes over the MRR, the extent of the vertical profiles is reduced due to low levels of SNR induced by signal attenuation. Although the IDRA radar shows the reflectivity field at much higher spatial resolution than the Herwijnen radar, the echoes behind the convective line seem to be attenuated. Thereby, a careful data processing is needed to be able to compare measurements from the different radars. The processing methodology is explained in the following sections.

b. DSD retrievals from MRR

The following describes the procedure for retrieving DSD profiles from MRR measurements (METEK 2015). A flowchart summarizing the essential steps is provided in Fig. 4. The procedure starts with a spectral reflectivity profile η (in m^{-1} Hz^{-1}) of size $n_g \times n_s$ obtained from attenuated power profiles averaged over 10 s. To express η in the velocity domain, η is divided by the Doppler velocity resolution Δv (m s^{-1}), where $\Delta v = \Delta f \times \lambda/2$ and λ (m) is the wavelength of the MRR. This leads to $\eta_a(i, v)$ in units of m^{-1} per m s^{-1} where a, i, and v denote attenuation, range gate index, and velocity, respectively. The drop size distribution $N_a(i, D)$ (m^{-3} mm^{-1}) derived from $\eta_a(i, v)$ is expressed as

$$N_a(i,D) = \eta_a(i,v)\frac{\partial v}{\partial D}\frac{1}{\sigma_D}, \tag{1}$$

where D (mm) is the volume-equivalent spherical drop diameter, $\partial v/\partial D$ is the derivative of the fall velocity with diameter, and σ_D (m^2) is the radar backscattering cross section of a raindrop of diameter D. For simplification purposes, all particles are assumed to be raindrops.

For the estimation of $\partial v/\partial D$, the fitted relation between the diameter of a raindrop and its fall velocity suggested by Atlas et al. (1973) is used:

$$D = \frac{1}{0.6}\ln\left(\frac{10.3}{9.65 - v}\right), \tag{2}$$

which leads to $(\partial v/\partial D) = 6.18\exp(-0.6D)$ (m s^{-1} mm^{-1}). In Eq. (2), it is assumed that v represents the terminal fall velocity of drops, neglecting any vertical wind component due to updrafts or downdrafts. In general, v should also be corrected for its dependency to air density at different heights. However, given the experimental setup and the fact that the maximum altitude is 900 m, such corrections are ignored here. Note that the relation between D and v is nonlinear and although Δv is constant in the MRR measurements, the spacing between two consecutive D values (i.e., ΔD in mm) corresponding to the retrievals is not uniform. Moreover, Eq. (2) cannot be applied for $v \leq 0$ or $v \geq 9.65$ m s^{-1} and, therefore, Peters et al. (2005) suggested a truncation of the Doppler range spectrum from 0.76 to 9.36 m s^{-1}, leading to a minimum diameter D_{min} of 0.25 mm and a maximum diameter D_{max} equal to 5.95 mm. This seems reasonable as the velocity resolution of the MRR is 0.19 m s^{-1} and the maximum measurable velocity is 12 m s^{-1}. More details on the importance of this truncation will be given in section 4.

To simulate σ_D, the numerical Fredholm Integral Method (FIM) (Holt and Shepherd 1979) is used so that scattering from the Mie regime is included. In the FIM model, σ_D is simulated according to the radar frequency (i.e., 24.15 GHz), incidence angle (i.e., 90°), axis ratio model, and temperature. The axis ratio is approximated by a hybrid drop shape model suggested by Otto and Russchenberg (2011) and the temperature is determined from the weather station, neglecting vertical variability. Once a profile of $N_a(i, D)$ is obtained, the specific attenuation $\kappa(i)$ and the path integrated attenuation PIA(i) are estimated in an iterative manner, starting from the range gate nearest to the radar where attenuation can be neglected (Peters et al. 2010). Because the first three range gates are within the near-field region of the antenna, the iteration process starts at $i = 4$ with PIA(i) = 1. Note that, PIA is given as a multiplicative factor. At $i = 5$, the specific attenuation is given

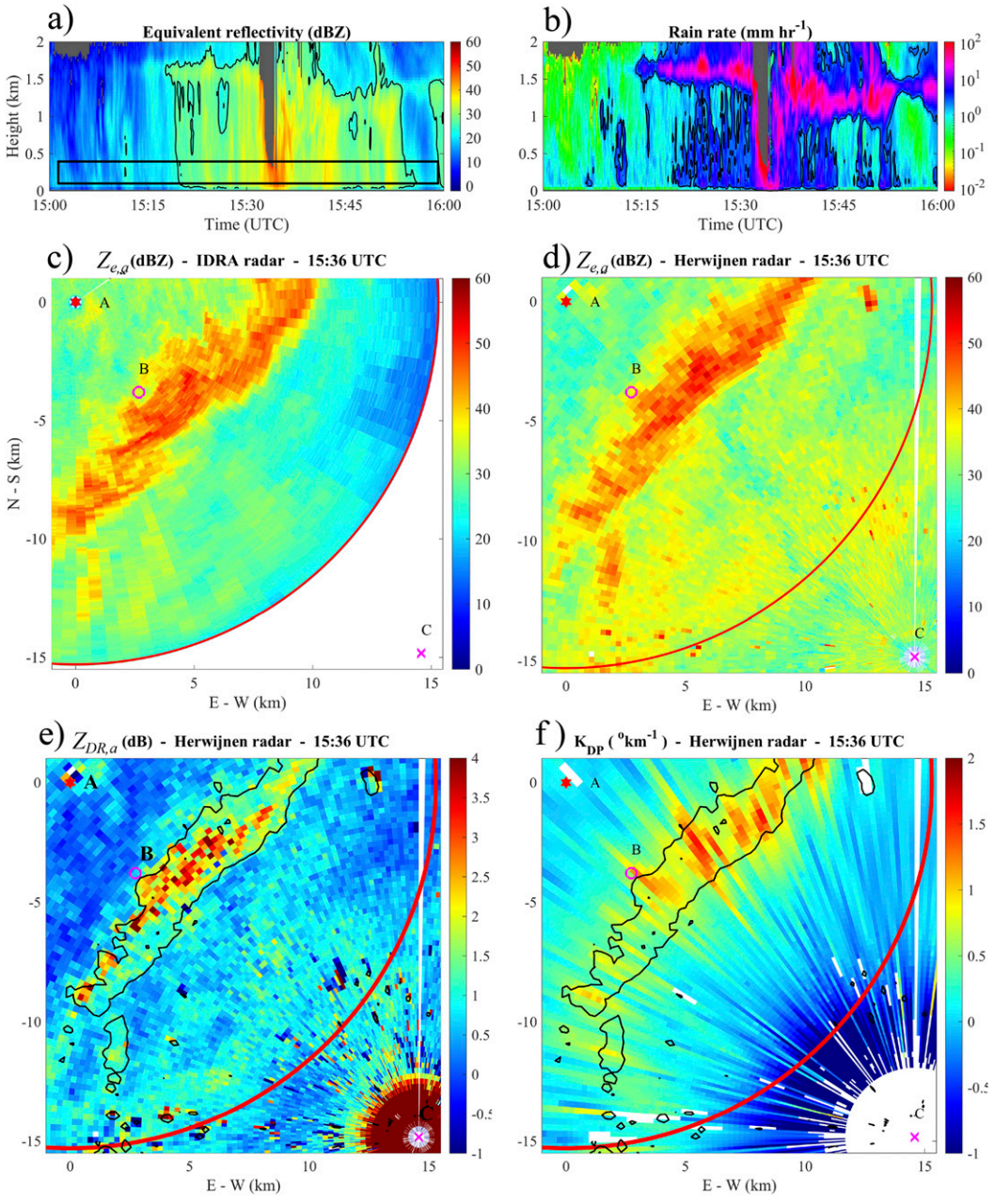

FIG. 3. Observations of the event E4 (7 Dec 2018) by the radar network. MRR profiles of (a) Z_e and (b) R. The black rectangle in (a) displays the range gates between 100 and 400 m. The black contours in (a) and (b) represent the 25 dBZ and the 2 mm h^{-1} levels, respectively. The gray areas in (a) and (b) indicate areas of low SNR. $Z_{e,a}$ from (c) IDRA and (d) Herwijnen radars at 0.5° and 0.8° elevation angles. Additionally, (e) $Z_{\mathrm{DR},a}$ and (f) K_{DP} from Herwijnen radar. The locations of the three radars are indicated by the points A (IDRA), B (MRR), and C (Herwijnen).

by $\kappa_o(i) = \mathrm{PIA}(i-1)\int_D N_a(i, D)\sigma_D^{\mathrm{ext}} dD$ (m^{-1}) where σ_D^{ext} (m^2) is the extinction cross section obtained from Mie-scattering theory (Doviak and Zrnić 1993). Next, PIA(i) is determined by $\mathrm{PIA}(i) = \mathrm{PIA}(i-1)\exp[2\Delta r_M \kappa(i)]$, where Δr_M is the MRR range resolution and $\kappa(i)$ is estimated in terms of $\kappa_o(i)$ according to the procedure described in Peters et al. (2010). This is repeated for successive values of i until PIA(i) reaches 10 and the DSD cannot be reliably estimated anymore (Peters et al. 2010). The final spectral reflectivity profile corrected for attenuation is given by $\eta(i, \upsilon) = \eta_a(i, \upsilon)\mathrm{PIA}(i)$, leading to an attenuation corrected estimate of the DSD given by

$$N(i, D) = \eta(i, \upsilon)\frac{\partial \upsilon}{\partial D}\frac{1}{\sigma_D}. \tag{3}$$

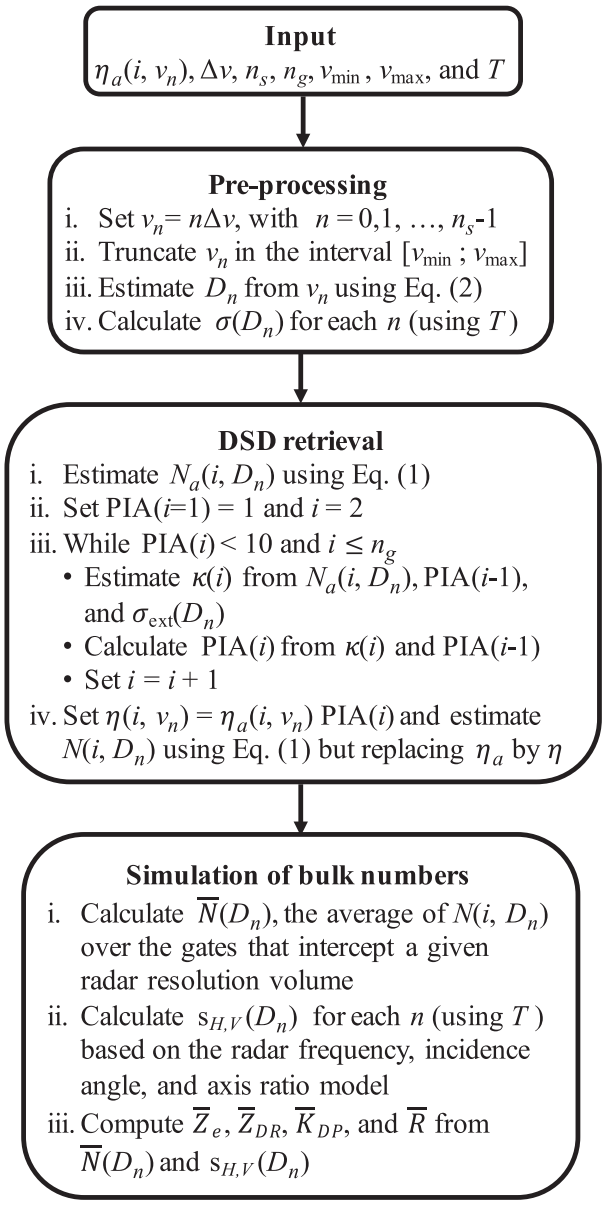

FIG. 4. Flowchart for the retrieval of DSD profiles from a MRR and for the simulation of radar polarimetric variables and rainfall rate, where $\eta_a(i, v_n)$ is the spectral reflectivity profile, Δv is the Doppler velocity resolution, n_s is the number of spectral samples, n_g is the number of range gates, v_{min} is the minimum Doppler velocity, v_{max} is the maximum Doppler velocity, and T is temperature. The path-integrated attenuation (PIA) is given in linear scale as a multiplicative factor.

c. Quality control of retrieved DSDs

Before the MRR retrievals can be compared to observations from scanning radars, a series of quality control steps are required to reduce possible sources of errors that can affect DSDs and thereby simulated radar observations in rain. First, DSDs resulting from the lowest three MRR gates (i.e., up to 70 m) are removed because of noise associated with the near field. Second, all DSDs resulting in estimates of $R < 0.1\ \mathrm{mm\ h^{-1}}$ are removed to limit noisy areas. Third, DSDs associated with PIA values >10 are also removed. Next, a filter is applied to discard all DSDs located in and above the melting layer (as detected by the MRR software). Last, DSDs that are associated with aliased Doppler spectra are identified and flagged. The identification of aliased spectra is based on the method introduced by Tridon et al. (2011). In this method, a spectrum is aliased if 8 or more spectrum samples of $\eta_a(v)$ fall outside the truncation interval $[v_{min}, v_{max}]$. However, this simple method is not sufficient in our case because the MRR-PRO provides Doppler samples of $\eta_a(v)$ that cover nearly the entire velocity domain (i.e., $0 < v < 12.3\ \mathrm{m\ s^{-1}}$). Thus, if we would apply the original method by Tridon et al. (2011), all spectra would be flagged as aliased. To avoid this, we only count the samples of $\eta_a(v)$ that are outside the truncation limit and whose value is larger than a given threshold. Based on the settings given in Table 1 and multiple observed spectra, the maximum number of samples outside the truncation was set to 12 while the threshold on $\eta_a(v)$ was set to $10^{-2}\ \mathrm{m^{-1}}$. These two parameters can be tuned by the user to reflect other sensors and measurement configurations. All DSDs corresponding to flagged Doppler spectra and the ones above them are removed from the profile and ignored during the comparisons.

d. Data processing for Herwijnen radar

The relevant measurements from the Herwijnen radar consist of attenuated reflectivity $Z_{e,a}$ (dBZ), attenuated differential reflectivity $Z_{DR,a}$ (dB), differential phase Ψ_{DP} (°), smoothed differential phase Φ_{DP} (°), specific differential phase K_{DP} (° km^{-1}), and cross-polar correlation coefficient ρ_{hv}. The details of how exactly K_{DP} is estimated are unknown to the authors due to protected information from the KNMI radar provider. However, we know that a least squares fit is conducted over a selected range path interval of Φ_{DP} similar to Bringi and Chandrasekar (2001). The slope of the fit is used as an estimate of K_{DP} for the gate centered at the path interval. Based on the segmented pattern seen in the K_{DP} field, the path interval seems to be in the order of 5 km. Ground clutter signals are mitigated operationally, using statistical filtering (Beekhuis and Holleman 2008).

Precipitation areas that may be associated with hydrometeors other than rain and/or nonmeteorological particles are filtered using measurements of the cross-polar correlation coefficient and reflectivity such that all range gates with $\rho_{hv} < 0.90$ or $Z_e < 0$ dBZ are removed (Ryzhkov and Zrnić 2005). The unwrapping on Φ_{DP} is done by adding −360° to Φ_{DP} for all gates with $\Phi_{DP} \geq 180°$. To obtain attenuation corrected reflectivity and differential reflectivity, Z_e and Z_{DR}, the method proposed by Bringi et al. (1990) is used such that the two-ways path integrated attenuation in reflectivity is estimated as $\mathrm{PIA}_H = \alpha\Phi_{DP}$ while the one in differential reflectivity is given by $\mathrm{PIA}_{DP} = \gamma \mathrm{PIA}_H$, where α and γ are constant coefficients. According to Bringi and Chandrasekar (2001), $\alpha = 0.073$ dB $(1°)^{-1}$ and $\gamma = 0.178$ are valid at C-band frequencies.

e. Data processing for IDRA radar

To avoid areas that include particles other than rain and/or areas with low SNR, measurements of linear depolarization

ratio L_{DR} (dB) are used, such that range gates with L_{DR} larger than −18 dB are discarded from the Ψ_{DP}, $Z_{e,a}$, and $Z_{DR,a}$ fields. Attenuation correction of $Z_{e,a}$ and $Z_{DR,a}$ is performed using the same procedure as for the Herwijnen radar but with $\alpha = 0.34\,\text{dB}\,(1^\circ)^{-1}$ and $\gamma = 0.147$ obtained from scattering simulation at X-band frequencies (Otto and Russchenberg 2011). For the purpose of attenuation correction, Ψ_{DP} is smoothed using a linear regression fit over a 3-km window along its radial. For the estimation of K_{DP} in rain, the approach proposed by Reinoso-Rondinel et al. (2018) is applied that performs an adaptive selection of the path interval to minimize contribution of the backscattering differential phase and random fluctuations on Ψ_{DP}. In addition, this approach uses the self-consistency principle introduced by Scarchilli et al. (1996) between Z_e, Z_{DR}, and K_{DP} to maintain the spatial variability of K_{DP} at range resolution scales.

f. *Simulation of polarimetric variables and comparative approach*

As illustrated in Figs. 1 and 2, the experimental setup allows one to collect measurements of precipitation from three independent radar systems (MRR–Herwijnen–IDRA) with overlapping sampling volumes. However, it is important to point out that since each radar operates at a different frequency, using different range resolutions, and sampling rates, one cannot just compare their measurements one-to-one and expect a perfect agreement. The main reason why DSDs play a crucial role in radar remote sensing is that most radar observables are just weighted statistical moments of the DSD, with some predefined weights depending on the scattering properties of raindrops at a given frequency, polarization, incidence angle, drop shape, and temperature. This means that if we know the DSD in a given volume of air, we can predict (with a fairly good level of approximation) what a radar with a given elevation angle, beamwidth, frequency, and polarization should measure (Testud et al. 2000; Park et al. 2005). In a similar manner, we can use the retrieved DSDs from the MRR to predict Z_e, Z_{DR}, and K_{DP} at C- and X-band frequencies. These simulated values can then be compared to the actual observations of the Herwijnen and IDRA radars to judge the quality of the DSD retrievals and quantify possible biases affecting these two radars.

The scattering properties of raindrops depend on many physical variables. The most important ones considered in this study are frequency, polarization, angle of incidence, drop axis ratio and temperature. The frequency, polarizations and incidence angles are chosen to match the characteristics of the Herwijnen and IDRA radars given in Table 1. For the drop axis-ratio model, we chose the hybrid ratio method suggested by Otto and Russchenberg (2011). The temperature is taken from the data recorded by the weather station. The scattering amplitudes at the horizontal and vertical polarization $s_{H,V}(D)$ that correspond to all these parameters are calculated using the FIM method (Holt and Shepherd 1979) to include scattering from the Mie regime in the forward and backward directions. Once the scattering amplitudes have been calculated and the $N(D)$ profiles have been retrieved from the MRR, radar observations of Z_e, Z_{DR}, and K_{DP} can be simulated. For the definition of these polarimetric moments in terms of $N(D)$ and $s_{H,V}(D)$, the reader is referred to Doviak and Zrnić (1993) and Testud et al. (2000).

In the case of the Herwijnen radar, the elevation angle of 0.8° was used as radar beams at lower elevation angles lead to unfiltered ground clutter echoes. Note that the $N(D)$ in the nine MRR gates between 105 and 385 m were averaged to obtain an average DSD $\overline{N}(D)$ that represents the DSD in the resolution volume. To better represent the DSDs within the resolution volume of the Herwijnen radar, the beam broadening effect from the Herwijnen radar can be considered, so that, the intercepted DSDs are multiplied by a beam weighting function (Gorgucci and Baldini 2015). However, given the short distance between the MRR and the Herwijnen radar (16.2 km) and the fact that the dwell times from each radar are different, such procedure is neglected here. For the IDRA radar, the elevation angle of 0.5° was used, corresponding to seven MRR gates between 140 and 350 m.

The described procedure is summarized in the last block of Fig. 4. In this way, simulated observations of Z_e, Z_{DR}, and K_{DP} from MRR can be compared with those measured by the Herwijnen and IDRA radar at their corresponding range and azimuth of interception (see Figs. 1 and 2). Note that, although the MRR provides Z_e profiles (i.e., without the need to retrieve DSDs), it should be pointed out that these values depend on the radar frequency. Therefore, the Z_e from the MRR are also simulated, matching the frequencies of the Herwijnen and IDRA radar.

In an effort to match the temporal resolutions from the two scanning radars as well as possible, only the simulated polarimetric parameters from the MRR observations for every 5 min (Herwijnen radar) and 1 min (IDRA radar) are considered during comparisons. More specifically, only the MRR profiles (generated at 10 s interval) closest to the registered scanning times are selected. This is possible because both scanning radars register the time of every scan in elevation. Because the internal clocks of the radars or the weather station were not synchronized, the samples were shifted in time before comparison assuming one of the systems (i.e., the operational Herwijnen radar) as the reference. This was done manually by comparing the two time series and finding the shift that maximizes the correlation.

To monitor the performance of the MRR in terms of rainfall rate, R values from the vertical range gate at 105 m was compared with in situ rainfall measurements acquired by the weather station. To obtain comparable values, R estimates from the MRR were averaged over the same time intervals as the gauge (5 min), taking 30 consecutive samples of 10 s rainfall rates.

4. Results and discussion

a. *Examination of polarimetric quantities derived from DSDs*

The main purpose of this section is to 1) illustrate the sensitivity of the simulated polarimetric variables to the DSDs retrieved from the MRR profiles and 2) compare the simulated

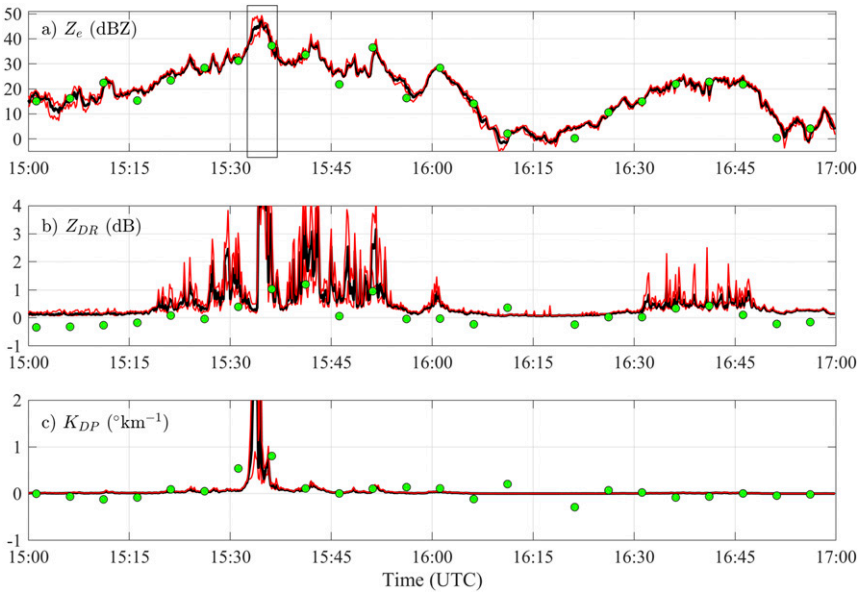

FIG. 5. Time series of (a) Z_e, (b) Z_{DR}, and (c) K_{DP} from the Herwijnen (green dots) and the MRR (continuous lines) radar on 7 Dec 2018, event E4. The black line in (a) represents the average Z_e while the red lines indicate the maximum and minimum Z_e within 105–385 m. In addition, the black rectangle indicates the time interval in which the convective line is observed by the MRR.

polarimetric radar quantities with the actual observations from the Herwijnen and IDRA radars.

Figure 5 shows the time series of Z_e, Z_{DR}, and K_{DP} of the MRR and Herwijnen radar for a 2-h interval in event E4. The black curves are obtained by averaging the DSDs in the intercepted resolution volumes, as explained in section 3f, while the red curves represent maximum and minimum polarimetric quantities from single MRR gates within the interception volume. Around 1533 and 1534 UTC, a small convective line passes the location of the MRR, as seen in Fig. 3, causing aliasing in the Doppler spectra that leads to Z_e values equal to 45 dBZ, Z_{DR} of at least 4 dB, and K_{DP} as high as 9.2° km^{-1}. To illustrate the impact of aliasing on retrieved DSDs from the MRR, Figs. 6a and 6b show the attenuated spectral reflectivity and the retrieved drop size distributions, respectively. The two plus signs in Fig. 6a indicate the truncation of the Doppler range (left $v = 0.76\,\mathrm{m\,s^{-1}}$ and right $v = 9.36\,\mathrm{m\,s^{-1}}$) in which DSDs and their moments are retrieved. At 1532 UTC, the shapes of the retrieved DSDs are very similar except for drop sizes larger than 4 mm, which may indicate a slight vertical variability of large drops or small errors during the conversion of terminal velocity to drop diameter. Note that the spacing in D is not uniform and increases with D. At 1533 UTC, the peaks of the spectra at heights of 245 and 350 m shift to the left (i.e., toward smaller Doppler velocities). The most likely reason for this is a vertical updraft that slows down the fall velocity of the raindrops. The aliased spectra led to inaccurate DSD estimates as shown in Figs. 6d and 6f. The apparent high contribution of small drop sizes results in nonphysical values of rainfall rates on the order of a few hundred millimeters per hour, which are much larger than those recorded by the weather station. Other moments such as the mass-weighted mean diameter and Z_e however, are still plausible but inaccurate, reaching values of 3 mm and 45 dBZ. In other words, the aliasing in Doppler spectra $\eta(v)$ might not necessarily be visible based on reflectivity values alone. In the following, aliased spectra were identified and removed as explained in section 3c.

In Fig. 5, $\eta(v)$ is truncated from the maximum velocity of 12.3 to $9.36\,\mathrm{m\,s^{-1}}$ (equivalent to $D = 5.95$ mm). The same simulated variables are shown in Fig. 7 but using a lower maximum Doppler velocity threshold of $9.0\,\mathrm{m\,s^{-1}}$ (equivalent to $D = 4.3$ mm). With this new threshold, the retrieved DSD loses two diameter classes. While the time series of Z_e and K_{DP} remain almost unchanged, Z_{DR} values are between 0 and 2 dB with substantially lower temporal variability than in Fig. 5. This shows that Z_{DR} is very sensitive to the presence of large drops, estimated in Eq. (2), even if their contribution to the total DSD is not substantial. By contrast, Z_e and K_{DP} also depend on the number concentration (Zrnić and Ryzhkov 1999). The conclusion is that for a stable simulation of Z_{DR} using the MRR, the right side truncation of $\eta(v)$ is very important and a slightly lower threshold of $9.0\,\mathrm{m\,s^{-1}}$ instead of $9.36\,\mathrm{m\,s^{-1}}$ is suggested. Nevertheless, one has to be careful when using this lower threshold. For example, in events with drop diameter larger than 4.3 mm, such threshold can lead to underestimated values of simulated Z_{DR}. Hereafter, the simulation of Z_e, Z_{DR}, and K_{DP} will be associated with the suggested threshold of $9.0\,\mathrm{m\,s^{-1}}$.

Note that the time series of simulated Z_e, Z_{DR}, and K_{DP} seem to be consistent among each other and also with those obtained from the Herwijnen radar. For example, the simulated Z_e can capture the temporal variability of the observed

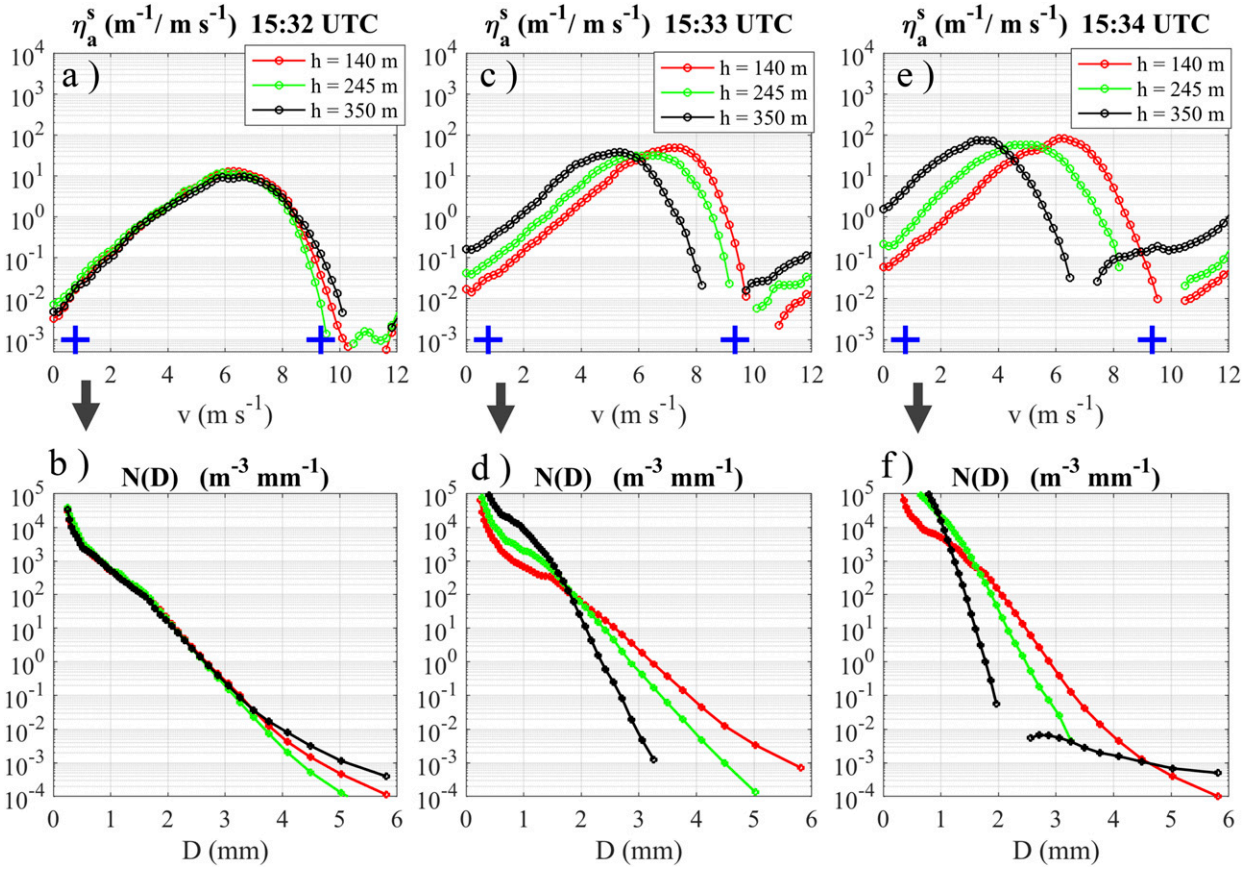

FIG. 6. Examples of retrieved DSDs from the MRR at (left) 1532, (center) 1533, and (right) 1534 UTC 7 Dec 2018, event E4. (a),(c),(e) The attenuated spectral reflectivity as a function of Doppler velocity at 140 (red), 245 (green), and 350 (black) m, where $\eta_a^s = 10^6 \eta_a$; (b),(d),(f) the corresponding drop size distributions as a function of D. The two plus signs indicate the truncation of the Doppler range: $v = 0.76\,\mathrm{m\,s^{-1}}$ for the left plus sign and $v = 9.36\,\mathrm{m\,s^{-1}}$ for the right plus sign.

Z_e in the range of 0–40 dBZ. In the case of K_{DP}, the variability is reduced and most of the observed and simulated samples are near $0°\,\mathrm{km^{-1}}$, except during 1530–1540 UTC. The correlation between the Z_{DR} values from the MRR and Herwijnen radar for event E4 is equal to 0.86. However, it seems that Z_{DR} values from the Herwijnen radar are biased, resulting in $Z_{DR} < 0$ dB during light rain while the expected value should be ~0 dB. More analysis on bias correction will be shown in section 4b.

Figure 8 shows time series of Z_e, Z_{DR}, and K_{DP} of the MRR and IDRA radar for a 2-h interval in event E1. Event E1 mostly consists of stratiform rain with a persistent melting layer identified at a height of approximately 1.5 km. The simulated time series were obtained after applying the quality control procedure and truncation of $\eta(v)$ to $9.0\,\mathrm{m\,s^{-1}}$. Note that the time series from IDRA are at a high temporal resolution of 1 min, which offers more data for comparison with the MRR. The temporal variability of Z_e seen by IDRA is consistent with the simulated values of Z_e from the MRR. It is also noticeable that during this event, the simulated time series of Z_e are slightly larger than those observed by IDRA, which was not the case for the Herwijnen radar. This could mean that the Z_e from IDRA is biased (i.e., underestimated). A similar conclusion is reached when comparing simulated and observed values of Z_{DR}. In this case, IDRA seems to be affected by a bias in Z_{DR} (i.e., overestimated). Indeed, values of Z_{DR} in the range of 0.5–1.0 dB can be seen in time intervals associated with light rain, suggesting that IDRA may not be well calibrated, consistent with the study by Otto and Russchenberg (2011). An in-depth analysis of the radar calibration of IDRA and Herwijnen is beyond the scope of this work. However, observations from the MRR suggest that both radars suffer from biases (see section 4b for more details). Observations from the Herwijnen radar in event E1 (not shown here) indicate that measurements of Z_{DR} are affected by a negative bias, similar to the one seen in event E4. This shows the potential of using the MRR to detect and monitor possible calibration biases in Z and Z_{DR} resulting from scanning radars that are operating continuously. At the same time, it is also important to closely monitor the measurements given the MRR, especially when the system has been operating for a considerable long period of time without maintenance, which can increase its aging and reduce its reliability. For this, it is convenient to collocate the MRR

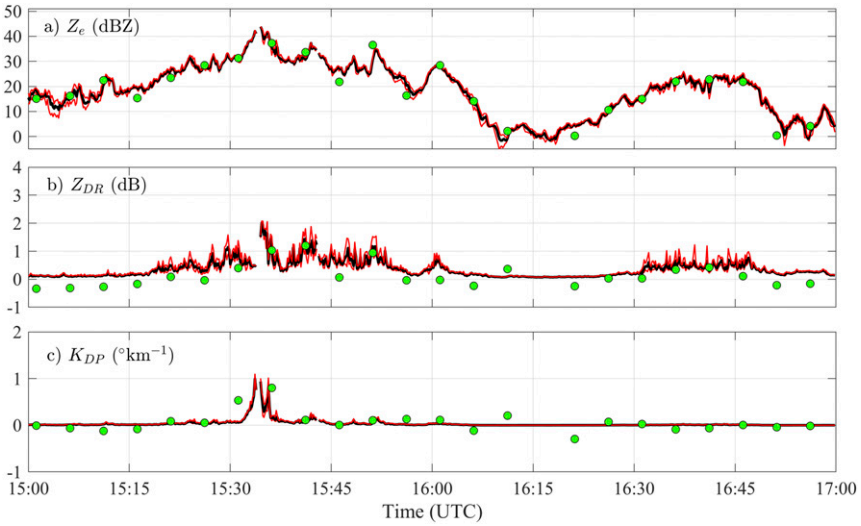

FIG. 7. As in Fig. 5, but after removing the aliased spectra and shortening v_{max} from 9.3 to 9.0 m s^{-1} during the retrieval of the DSDs.

with ground-based sensors such as rain gauges or disdrometers. In our case, the MRR-PRO was still new and had been recently calibrated by METEK. The measurements it provided were in good agreement with the rain gauge. Therefore, in this work, one can assume that the MRR is well calibrated at the time of the experiments. By contrast, the IDRA radar system has been operating since 2008 while the Herwijnen radar was installed and upgraded with polarimetric capabilities in 2016.

Similar to event E4, the K_{DP} time series in event E1 is close to 0° km^{-1}, except at 0607 UTC, when Z_e reached a maximum value near 40 dBZ and the estimated and simulated K_{DP} samples increased to 1.0 and 0.5° km^{-1}, respectively. Estimates of K_{DP} in areas with $Z < 30$ dBZ are typically very noisy and often need range smoothing. However, those from IDRA are estimated at a range resolution of 30 m and it can be seen that they slightly fluctuate around the ones retrieved from the MRR, with a root-mean-square difference (RMSD) equal to 0.20° km^{-1}. Because of the short duration of the experiment and its timing during the winter season, very few large values of K_{DP} were observed. Even so, the MRR can provide a high-resolution K_{DP} reference that can be used to analyze the performance of estimated K_{DP} values, especially the impact of range smoothing that usually leads to the underestimation of K_{DP} peaks. One issue, however, is that periods corresponding to large K_{DP} values are likely to contain aliased Doppler spectra.

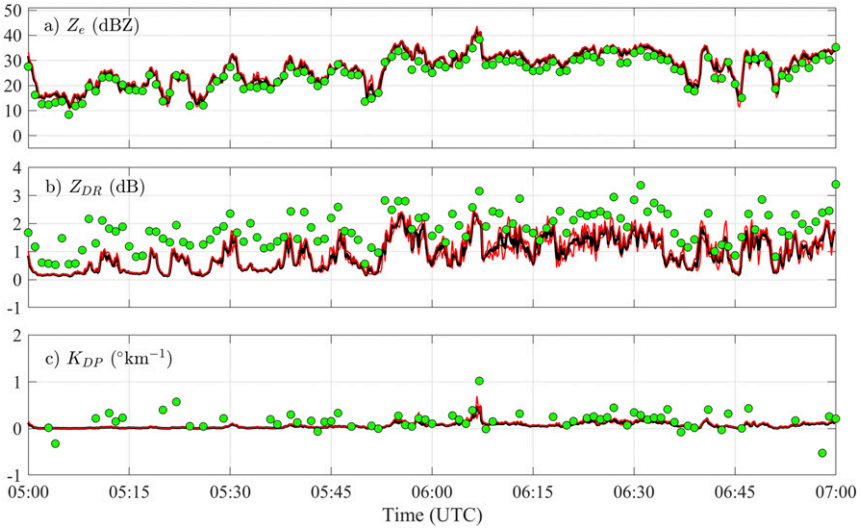

FIG. 8. As in Fig. 7, but for the IDRA radar and event E1, 11 Nov 2018. The range gates from the MRR radar are within 140 and 350 m.

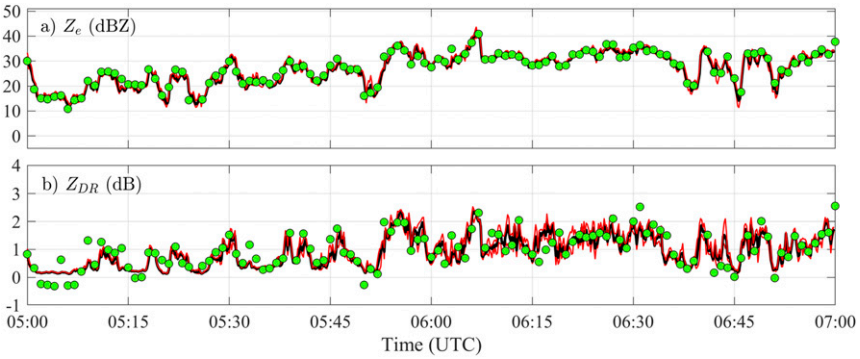

FIG. 9. As in Fig. 8, but after adjusting Z_e and Z_{DR} for bias.

b. *Bias correction in Z_e and Z_{DR}*

The bias correction in Z_e and Z_{DR} is denoted by B (dB) and is calculated by taking the difference between the arithmetic mean values of the simulated and observed samples in logarithmic scale. In the case of IDRA and event E1, for instance, this leads to a bias correction in Z_e equal to 2.45 dB and a bias correction in Z_{DR} equal to −0.84 dB. Figure 9 shows the time series of Z_e and Z_{DR} from IDRA after bias correction. The temporal consistency between estimated and simulated measurements is high. For Z_e, the Pearson correlation coefficient (ρ) and RMSD are equal to 0.96 and 1.80 dB while for Z_{DR} they are equal to 0.83 and 0.35 dB, respectively. The residual discrepancy can be due to the small mismatch between the resolution volumes and temporal sampling as well as the used approximations when retrieving DSDs and simulating scattering amplitudes. In the case of IDRA, it is known that measurements of Z_{DR} suffer from a radial pattern that adds a small oscillation to Z_{DR} over time (Reinoso-Rondinel et al. 2018). The radial pattern is probably due to a metallic fence that surrounds the IDRA platform. This introduces an azimuthal-dependent oscillation in the Z_{DR} field in a similar way as partial beam blockage effects (Giangrande and Ryzhkov 2005; Gourley et al. 2006; Vulpiani et al. 2012). For example, Gourley et al. (2006) realized that a security metallic fence, which surrounds a radar installed in the top of a tower in France, and an adjacent electronic box introduced bias on Z_{DR} that varies along azimuth. Vulpiani et al. (2012) also observed that Z_{DR} measurements obtained in Italy were characterized by an azimuthal modulation behavior due to nearby obstacles such as fencing and lightning rods.

Even though several issues related to scanning radars such as strong attenuation, partial beamfilling, and beam blockage were "avoided" due to the proximity of the MRR to the radars; hydrometeors other than rain can negatively impact the agreement of simulated observations and affect the bias correction. For instance, observations from the MRR in event E13 during 0600–1000 UTC reveal a low melting layer, approximately between 300 and 600 m, as shown in Fig. 10. In multiple instances, measurements from the Herwijnen radar, in which $Z_e > 0$ dBZ, show noisy values of ρ_{hv}, between 0.8 and 1.0, over and around the location of the MRR. Unfortunately, a simple minimum threshold of $\rho_{hv} = 0.90$ is not sufficient to classify particles as rain, mainly during wintertime. This can be seen on the ρ_{hv} and $Z_{DR,a}$ fields from the Herwijnen radar at 0736 UTC, displayed in Figs. 10b and 10c, respectively. Note that, the $Z_{DR,a}$ field is filtered using the constraint of $\rho_{hv} < 0.90$. Figure 11 shows a 2-h interval of event E13 to display how this might impact Z_e and Z_{DR}. The vertical variability of the simulated Z_e values is noticeable by its maximum and minimum values, with differences reaching values of up to 6 dBZ. This may be due to the incorrect application of the relation between fall velocity and particle diameter as well as the assumptions made during the scattering simulations. Nonetheless, the average resulting Z_e samples from the MRR and the measured ones from the Herwijnen radar are reasonably consistent. Measurements of Z_{DR} by the Herwijnen radar show significant variability in the range of −0.5 to 3.0 dB, which could indicate the presence of melting oblate-shaped ice particles, whereas those simulated by the MRR display a constant value for Z_{DR} near 0 dB. Although, the quality control process is able to detect gates associated with the melting layer, it is not able to distinguish rain from other hydrometeors. For this reason, all intercepted gates were used to simulate Z_e and Z_{DR} and no bias correction was attempted.

c. *Quantitative assessment of Z_e and Z_{DR}*

For a more general assessment of the MRR simulation chain and its capability of monitoring calibration biases from scanning radars, the same methodology to simulate and estimate Z_e and Z_{DR} using the MRR and both scanning radars was applied to all the events listed in Table 2. This includes the truncation of $\eta(v)$ to 9.0 m s^{-1} as well as the bias estimation and correction on Z_e and Z_{DR} measured by the Herwijnen and IDRA radar. The agreement was quantified in terms of ρ, RMSD and bias B. The results of this analysis are given in Table 3, which is divided into two groups: Z_e and Z_{DR}.

Recall that the events E10 and E13 (highlighted in bold) are related to a low melting layer (<600 m) and Z_e values smaller than 25 dBZ, possibly resulting from snow or a mix of hydrometeors with low concentration. Therefore, the presented method to simulate Z_e and Z_{DR} from retrieved DSD profiles may not be correct. This is confirmed by the low correlation coefficient associated with Z_{DR} ($\rho < 0.11$) resulting from the

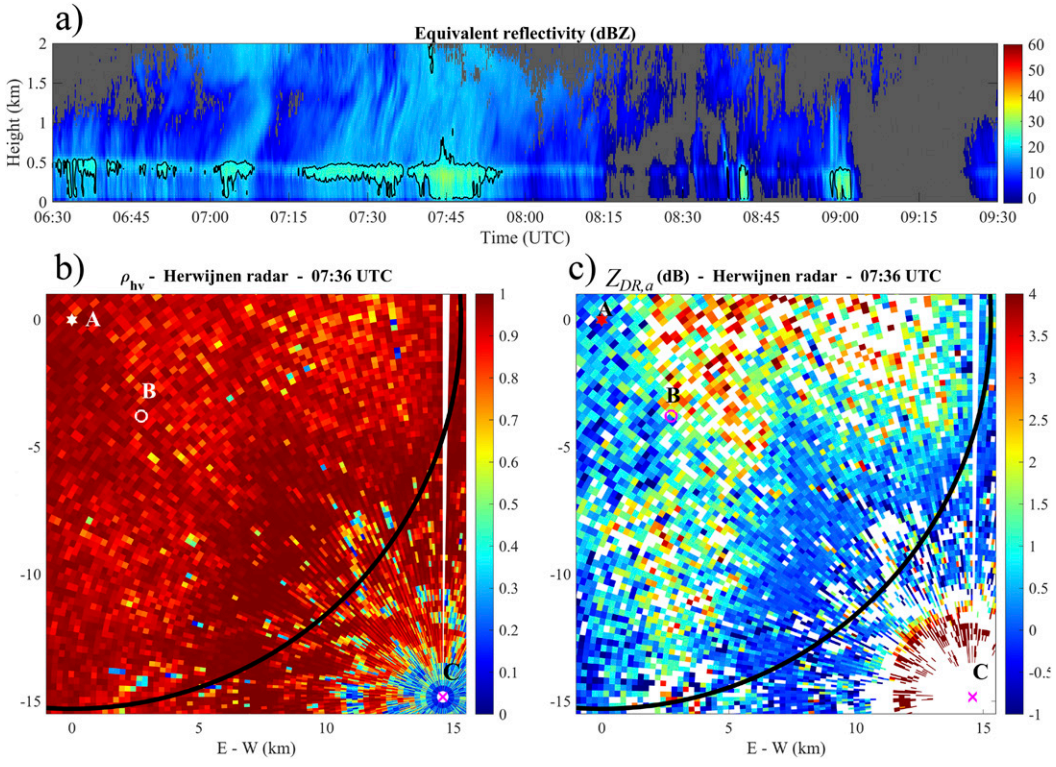

FIG. 10. Observations of the event E13 (28 Jan 2019) by the radar network. (a) MRR profiles of Z_e. The black contours in (a) represent the 20 dBZ level. (b) ρ_{hv} and (c) $Z_{DR,a}$ from the Herwijnen radar. Note that the $Z_{DR,a}$ field is filtered using the constraint of $\rho_{hv} < 0.90$. The location of the three radars are indicated by the points A (IDRA), B (MRR), and C (Herwijnen).

MRR-Herwijnen and MRR-IDRA comparison in both events. Also, the MRR-IDRA comparison of Z_e show lower accuracy during these two events, with $\rho < 0.65$ and RMSD > 5.00 dB. Note that in Table 3, the results associated with the IDRA radar in events E4, E5, E7, E9, E14, and E15 are missing. This is because IDRA suffers from an unstable power connection in which the radar stops measuring or the data quality decreases. This means that IDRA requires a close monitoring and a manual restart to avoid data gaps but unfortunately it is not always possible to succeed.

1) ASSESSMENT OF Z_e

Table 3 shows that Z_e values from the MRR and Herwijnen radar are well correlated ($\rho > 0.73$, excluding events E10 and E13) but the estimated RMSD varies between 1.44 and 4.67 dB. The events with RMSD < 2 dB and $\rho > 0.95$ are E3,

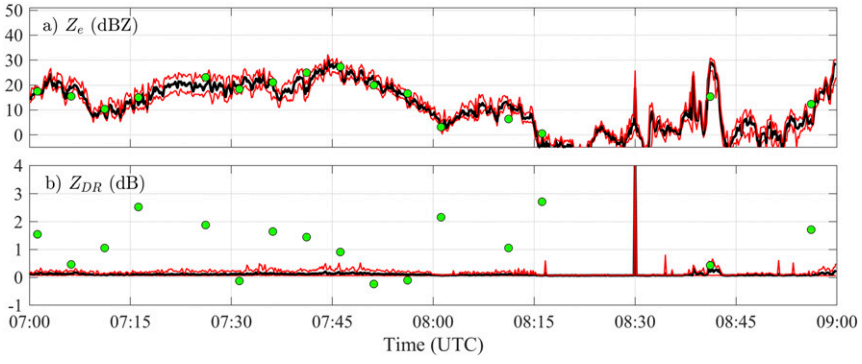

FIG. 11. Time series of (a) Z_e and (b) Z_{DR} (without bias correction) from the MRR and the Herwijnen radar on 28 Jan 2019, event E13. The Z_{DR} values are inconsistent with each other due to the low melting layer. The range gates from the MRR radar are within 105 and 385 m.

TABLE 3. RMSD, bias B, and correlation coefficient ρ for Z_e and Z_{DR} between MRR and both Herwijnen (C-band at 0.8° elevation angle) and IDRA (X-band at 0.5° elevation angle) radars. Note that events E10 and E13 are characterized by a low melting layer.

	Reflectivity Z_e						Differential reflectivity Z_{DR}					
	Herwijnen			IDRA			Herwijnen			IDRA		
Event	ρ	RMSD (dB)	B (dB)	ρ	RMSD (dB)	B (dB)	ρ	RMSD (dB)	B (dB)	ρ	RMSD (dB)	B (dB)
E1	0.93	2.29	−1.49	0.93	2.46	2.33	0.72	0.29	0.40	0.76	0.38	−0.84
E2	0.81	3.32	2.80	0.93	1.83	2.23	0.59	0.33	0.07	0.67	0.39	−1.04
E3	0.99	1.61	0.60	0.95	2.78	3.04	0.77	0.24	0.28	0.76	0.36	−0.98
E4	0.95	1.84	0.74				0.82	0.21	0.36			
E5	0.91	3.33	0.97				0.68	0.40	0.34			
E6	0.91	3.78	1.03	0.79	4.70	2.99	0.72	0.34	0.20	0.44	0.49	−0.97
E7	0.97	1.83	−0.02				0.73	0.24	0.32			
E8	0.97	2.53	0.93	0.98	1.87	2.81	0.87	0.32	0.26	0.86	0.42	−0.82
E9	0.73	4.67	2.17				0.40	0.37	0.24			
E10	**0.85**	**4.29**	**−0.62**	**0.50**	**7.03**	**2.99**	**0.11**	**0.59**	**−0.61**	**0.01**	**0.39**	**−0.83**
E11	0.95	1.44	0.43	0.96	1.07	3.25	0.89	0.14	0.44	0.70	0.37	−0.52
E12	0.96	2.51	0.76	0.86	4.17	3.00	0.72	0.26	0.29	0.54	0.62	−0.84
E13	**0.85**	**3.68**	**1.33**	**0.65**	**5.02**	**2.21**	**−0.07**	**0.75**	**−0.30**	**−0.15**	**0.91**	**−1.22**
E14	0.97	1.97	1.16				0.59	0.27	0.25			
E15	0.97	2.18	−0.04				0.82	0.30	0.22			

E4, E7, E11, and E14. These events were related to stratiform rain type with relatively high melting layer, Z_e values between 20 and 40 dBZ, and rainfall rates between 2 and 8 mm h^{-1}. The events with RMSD > 3 dB (E2, E5, E6, and E9) were associated with isolated rain areas passing over the MRR without any clear melting layer and Z_e values were weak. These events are likely to contain nonstationarities and rapidly changing microphysical processes that can lead to distinctive estimates of Z_e from both radar systems. In addition, it seems that the capability of the Herwijnen radar to detect small drops in light rain is less than that of the MRR. A scatterplot of Z_e values (not shown here) for event E9 shows that a whole group of Z_e samples, with $Z_e < 10$ dBZ, from the Herwijnen radar were smaller than those from the MRR, leading to the highest RMSD = 4.67 dB and lowest $\rho = 0.73$. During events E5 and E6, strong winds were recorded that could also increase the difference in Z_e from both radars.

From the bias values, the Herwijnen radar is affected by a bias between 0 and 1 dB, except for events E1, E2, and E9. As mentioned earlier, the conditions during events E2 and E9 were not favorable to obtain consistent estimates of Z_e from both radars. In event E1, most of Z_e values were larger than 20 dBZ and the melting layer was clearly visible. However, the estimated bias B was equal to −1.49 dB. This is because the MRR recorded rapid changes in Z_e (not necessarily wrong) in the order of 15–20 dBZ within 5 min. Such rapid fluctuations make it difficult to match the temporal (10 s against 5 min) and spatial resolution (35 m against 225 m) of the MRR and Herwijnen radar.

Based on the analysis between the MRR and IDRA radar, Z_e values are highly correlated ($\rho > 0.86$) and consistent, except in E6 where $\rho = 0.79$ (the lowest) and RMSD = 4.70 dB (the highest). In this event, the Z_e profiles were interrupted by several dry periods while the melting layer was not well identified. Also, Z_e values were found mainly between 10 and 30 dBZ in which the IDRA radar is sensitive to the noise level and interference from nearby telecommunication systems (Yin et al. 2019). Such interference is characterized by the flashy appearance, in light rain or no rain, of multiple radials with constant Z_e values that vary between −10 and 5 dBZ. This could explain the discrepancy of Z_e values quantified by ρ and RMSD. Another event with large RMSD is E12 (RMSD = 4.17 dB), which was characterized by weak values of Z_e and rainfall rates smaller than 3 mm h^{-1}. In terms of the bias B, IDRA seems to experience a systematic bias of ~2–3 dB. Note that the large temporal variability associated with event E1 did not impact the estimation of B as in the Herwijnen radar, most likely because the IDRA radar has a temporal resolution of 1 min, which makes it possible to see the temporal variability of Z_e as shown in Fig. 9.

2) ASSESSMENT OF Z_{DR}

A good correlation ($\rho \geq 0.68$) is found for the Z_{DR} values between the MRR and Herwijnen radar, except for events E2, E9, and E14 where $\rho \leq 0.59$. In these events, most of the wet periods were associated with rainfall rates less than 3 mm h^{-1} and Z_{DR} within 0 and 1 dB, which means that Z_{DR} is almost constant and makes it impossible to estimate the correlation coefficient. Only on a few occasions, the Herwijnen radar detected Z_{DR} values larger than 1 dB. This is possible because the resolution volume of the Herwijnen radar is much larger than that of the MRR, which increases the probability of detecting various drop sizes. The low RMSD (≤0.40 dB) indicates a reasonable spread between the Z_{DR} samples from the MRR and Herwijnen radar. In contrast to the observed low and high RMSD of Z_e, the impact of the mismatch between the spatial and temporal resolution of both radars as well as the unfavorable conditions such as interrupted rain periods, not well defined melting layer, and/or strong winds do not seem to considerably impact the RMSD of Z_{DR}. In consequence, the corresponding values for B vary only between 0 and 0.44 dB, indicating a small

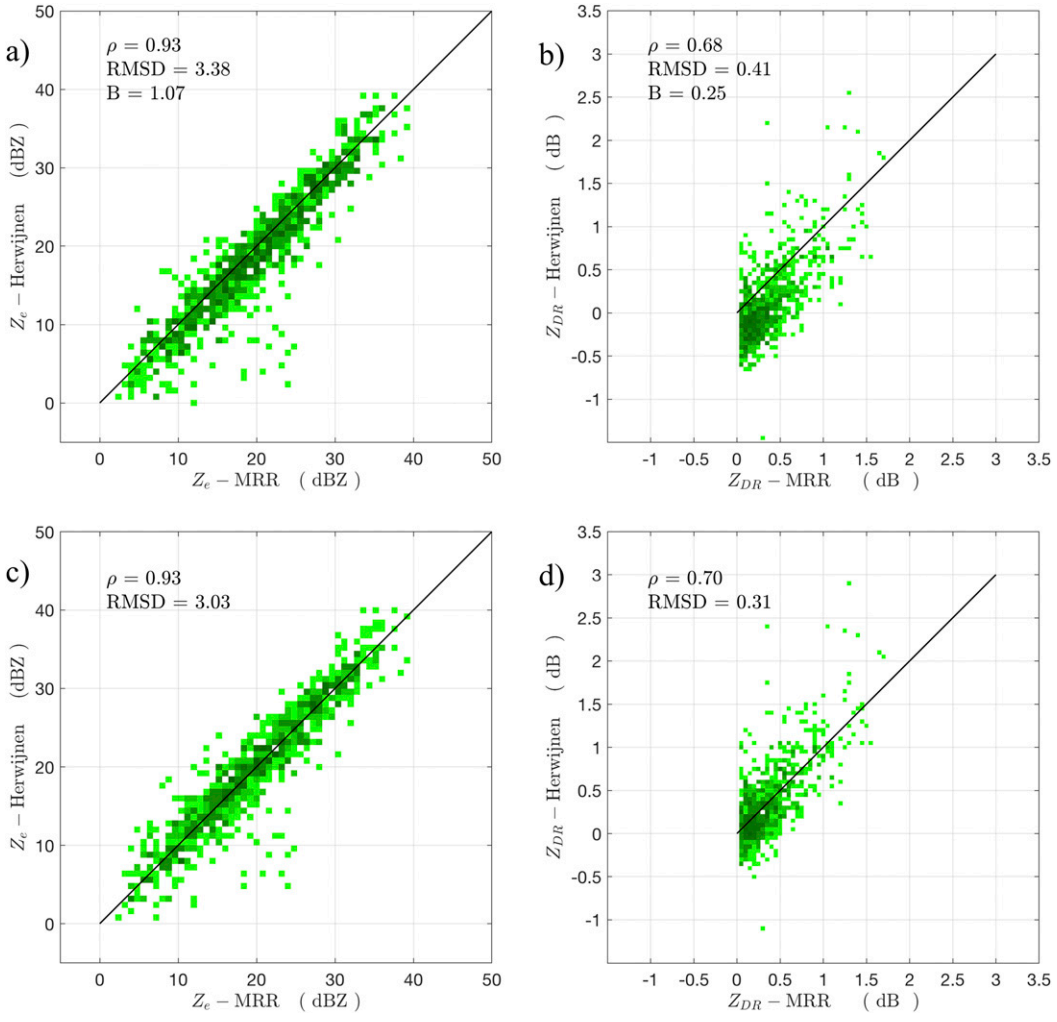

FIG. 12. Density of (a) Z_e–Z_e and (b) Z_{DR}–Z_{DR} from the MRR (x axis) and the Herwijnen (y axis) radars before bias correction. (c),(d) As in (a) and (b), but after bias correction. The RMSD and bias values were obtained from 815 pairs of measurements from the events given in Table 2, excluding E10 and E13.

Z_{DR} bias for the Herwijnen radar (i.e., Herwijnen underestimates Z_{DR}).

The comparison of Z_{DR} for the MRR and IDRA radar gives $\rho \geq 0.67$ and RMSD ≤ 0.42 dB, which is similar to the values obtained when comparing the MRR and Herwijnen radar. However, in events E6 and E12, the correlation decreased, $\rho \leq 0.54$, and the spread increased, RMSD ≥ 0.49 dB. As mentioned above, both of these events were associated with low rain rates in which the precision of the IDRA measurements is lower due to the unwanted radial pattern of Z_{DR}. Note that these events were also associated with increased RMSD values of Z_e between the MRR and IDRA radar. The average bias B in Z_{DR} is approximately equal to -1 dB.

To summarize the assessment of Z_e and Z_{DR}, Fig. 12 shows the scatterplot between the MRR and Herwijnen radar and Fig. 13 the one between the MRR and IDRA radar from the combination of the events listed in Table 3, except E10 and E13. For the Herwijnen radar, the bias in Z_e is equal to 1.07 dB while for Z_{DR} it is 0.25 dB. However, one has to take into account that the MRR measurement might not represent an absolute truth and thus the obtained bias should not be seen as an absolute calibration correction. Nevertheless, these biases are strong indications of calibration issues that should prompt KNMI to monitor the calibration of the Herwijnen radar. In the case of the IDRA radar, the bias in Z_e is equal to 2.67 dB while for Z_{DR} it is -0.93 dB. Note that after bias correction, the values of ρ and RMSD resulting from the MRR-Herwijnen are consistent with those from the MRR-IDRA comparison for both Z_e and Z_{DR}. However, note that the Z_{DR} scattering plot from the MRR-IDRA is more dispersed than that of the MRR-Herwijnen as expressed by their RMSD values. This might be due to the azimuthal oscillation that affects observations of Z_{DR} by the IDRA radar, resulting from the metallic fence that surrounds the radar platform. Although ρ values are on the order of 0.90 for Z_e and 0.70 for Z_{DR}, the observed statistical dispersion is inherent to the different radar resolution volumes

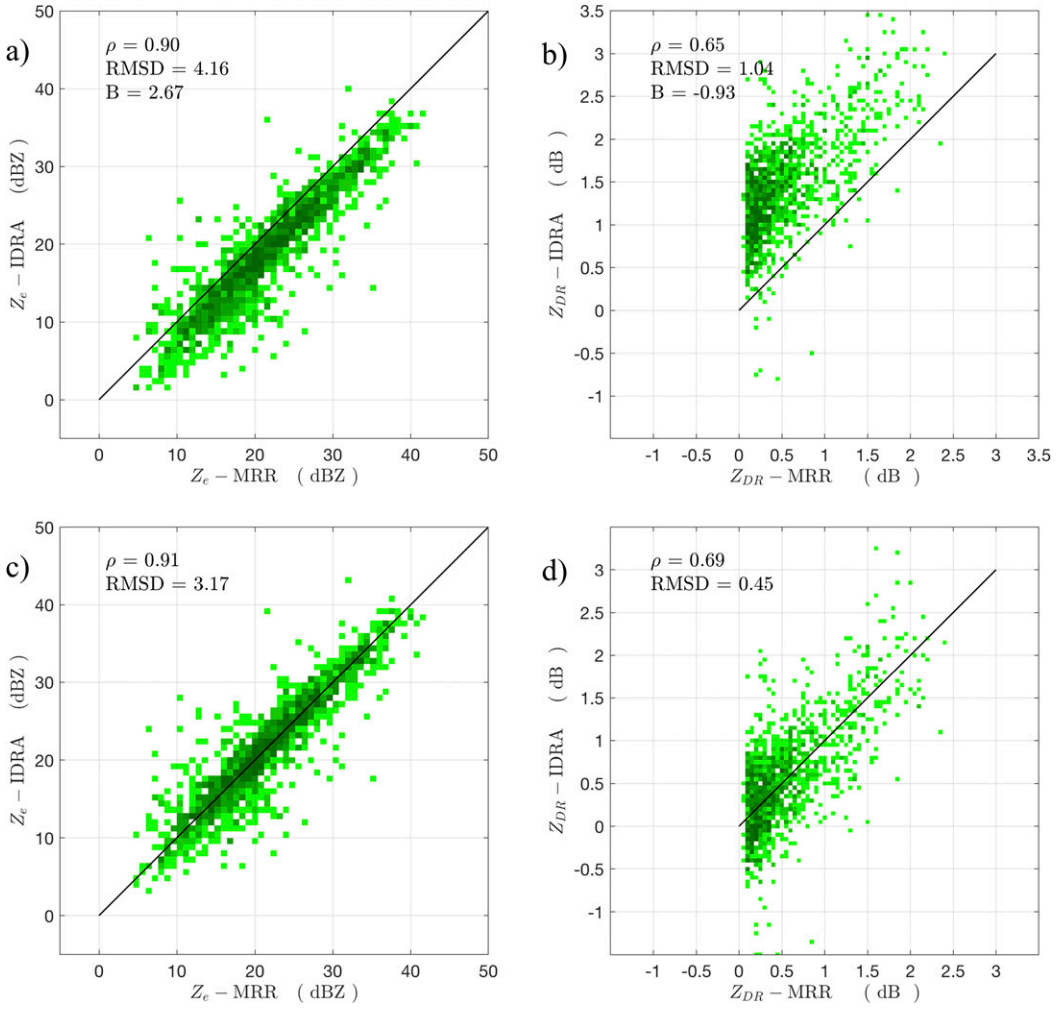

FIG. 13. As in Fig. 12, but for the MRR and the IDRA radar. A total of 1344 pairs were used from 7 events (E1, E2, E3, E6, E8, E11, and E12).

and the weather conditions, such as light rain, episodes of intermittent, and rapidly changing microphysical processes. This should aware one to expect a similar dispersion of observables that are derived from Z_e and/or Z_{DR} such as rainfall rate resulting from at least two independent radar systems.

5. Conclusions

In the last decades, many scanning weather radars have been upgraded from single to dual polarization, which makes it possible to retrieve more detailed information about precipitation hydrometeors. However, polarization measurements such as reflectivity Z_e and especially differential reflectivity Z_{DR} depend, among other factors, on how well a radar is calibrated. Therefore, it is important to monitor the accuracy of such measurements. Vertically pointing Micro Rain Radars can help with this task thanks to their capability to retrieve vertical profiles of raindrop size distribution over time. However, MRR retrievals can be affected by multiple errors due to aliasing and attenuation. In this work, we explored the possibility to use an MRR to assess the accuracy of operational scanning radars in rain by carefully retrieving DSDs and using them to simulate polarimetric observables such as Z_e, Z_{DR}, and K_{DP}. For such purpose, an MRR was installed between two nearby scanning radars, one at C-band and one at X-band frequencies, in a flat and rural terrain in the Netherlands, thereby reducing issues related to ground clutter, beam blockage, beamfilling, and attenuation.

One of the first issues that we investigated was the retrieval of DSDs from profiles of Doppler spectra. During the retrieval, a crucial step was to relate the raindrop terminal velocity to raindrop diameter. This step is sensitive to Doppler aliasing and hydrometeors from the melting layer. Several examples of aliased Doppler spectra that led to nonphysical values of rainfall rate and Z_{DR} were identified. An important point here is that Z_e values in aliased spectra can still be realistic, yet inaccurate. A quality control step was included to identify the lowest gate showing either

Doppler aliasing, echoes from the melting layer, or a PIA value larger than 10 dB, which greatly increased the reliability of the retrievals. Another challenge that we found was related to the simulation of Z_{DR}. We determined that Z_{DR} is very sensitive to the presence of large drops, even if their contribution to the total DSD is not significant. Knowing that large drops above 5.0 mm are very rare in the Netherlands during the winter period, we decided to truncate the right-hand side of the Doppler spectrum to 9.0 m s^{-1}, which is equivalent to a raindrop size of 4.3 mm. This leads to more accurate and less noisy Z_{DR} retrievals. In contrast, the sensitivity of Z_{DR} to temperature, raindrop axis ratio model, and the minimum raindrop size was much lower.

The time series of simulated Z_e, Z_{DR}, and K_{DP} were compared with those resulting from the Herwijnen and IDRA radar at elevation angles of 0.8° and 0.5°, respectively. The results indicated a good consistency in which the temporal variability of the polarimetric variables, mainly Z_e and Z_{DR}, observed by the scanning radars was well captured by those simulated from the MRR. This was easier to see for the IDRA radar than for Herwijnen due to the shorter revisit time (1 vs 5 min). To assess the capability of the MRR to monitor the calibration of both scanning radars, Z_e and Z_{DR} from 13 events observed by the Herwijnen and IDRA radar were compared against those simulated by the MRR. Results showed that 1) Z_{DR} values from the Herwijnen radar were negative in light rain while those from the IDRA radar were slightly large than 0 dB and 2) K_{DP} values resulting from the MRR were consistent with K_{DP} from both scanning radars. From the comparison between the Herwijnen and MRR radar, it was seen that Z_e and Z_{DR} were affected by biases of 1.07 and 0.25 dB, respectively. The correlation coefficient ρ and RMSD of Z_e from both radars were 0.93 and 3.03 dB. In the case of Z_{DR}, ρ and RMSD were equal to 0.70 and 0.31 dB, respectively. Such statistical values seem plausible considering the different sampling volumes and the presence of a few outliers related to episodes of intermittent, light rain, wind shear, and hydrometeors other than raindrops. In the case of the IDRA radar, the bias on Z_e was equal to 2.67 dB with $\rho = 0.91$ and RMSD = 3.17 dB. Measurements of Z_{DR} were associated with a bias of −0.93 dB with ρ and RMSD of 0.69 and 0.45 dB, respectively. As indicated before, the analysis on K_{DP} did not show such bias, which confirms that measurements of K_{DP} are less sensitive to radar calibration bias. However, the range of K_{DP} was limited due to the fact that most of the rain events were associated with rainfall rates less than 10 mm h^{-1}.

Several issues could limit the potential and effectiveness of using MRRs for the monitoring of scanning radars. The first concerns the presence of solid or mixed-phase precipitation. The presence of such particles could lead to erroneous MRR-based DSDs and misinterpretation of the results when comparing data from independent sources. The distance between a scanning radar and the MRR could also influence the analysis. A large distance can lead to observations from or near the melting layer and/or an increased discrepancy of observations from nonstationary events, in which microphysical processes vary rapidly in space and time, exacerbating the spatial and temporal resolution mismatch among radars. At long ranges, the effects of partial beamfilling on radar measurements could also increase. Last, one has to take into account that the accuracy and reliability of the attenuation correction algorithms used in the MRR and in the scanning radars decrease with the distance from the radar. Despite these limitations, the MRR is a remarkably robust and reliable sensor that gives valuable insight into vertical profiles of reflectivity and microphysical processes in rain. Future research should focus on improving the quality and consistency of the retrieved data using external information from independent sensors.

Overall, we can say that MRR measurements are useful to monitor and inspect the calibration of scanning radars, provided that the DSD profiles are accurately retrieved and controlled for quality assurance. This can be challenging during convective events where Doppler spectra tend to be affected by aliasing, leading to erroneous DSDs. However, the detection and correction of spectrum aliasing can be mitigated, for instance, by collocating the MRR with a cloud radar or a 3D wind profiler or by using the observations from scanning radars to shift the spectra of the MRR until the simulated Z_{DR} or K_{DP} are consistent with those from the scanning radars. One has to be aware that the MRR measurements can also be affected by errors and biases. The latter can be assessed with the help of collocated weather stations and disdrometers. Having more detailed ground-based observations would make it easier to quality control and validate the retrieved DSDs near the ground. Although, more tests are necessary in convective environments, the operational and research weather radar communities can already benefit from the proposed method to detect calibration biases and validate polarimetric estimates in rain.

Acknowledgments. Gratitude to 4TUDatacentrum for its support on keeping IDRA data an open access dataset and Dr. Tiemo Mathijssen from the KNMI institute for its support and discussion on the Herwijnen radar variables. The authors also thank to the management team of the camping ''De Victorie'' for allowing the installation and operation of the MRR. This work was supported by the MUFFIN project through ERA-NET and Water JPI, the climate institute of the Delft University of Technology, and the Ruisdael Observatory Project.

Data availability statement. The IDRA dataset is available from the 4TUDatacentrum repository at https://opendap.tudelft.nl/thredds/catalog/IDRA/catalog.html while the Herwijnen dataset is found at https://data.knmi.nl/datasets. The MRR and the weather station dataset are available upon request by contacting the authors of this work.

REFERENCES

Adirosi, E., L. Baldini, N. Roberto, P. Gatlin, and A. Tokay, 2016: Improvement of vertical profiles of raindrop size distribution from Micro Rain Radar using 2D video disdrometer measurements. *Atmos. Res.*, **169**, 404–415, https://doi.org/10.1016/j.atmosres.2015.07.002.

——, ——, and A. Tokay, 2020: Rainfall and DSD parameters comparison between Micro Rain Radar, two-dimensional

video and Parsivel disdrometers, and S-band dual-polarization radar. *J. Atmos. Oceanic Technol.*, **37**, 621–640, https://doi.org/10.1175/JTECH-D-19-0085.1.

American Meteorological Society, 2019: Rain. Glossary of Meteorology, http://glossary.ametsoc.org/wiki/Rain.

Atlas, D., R. C. Srivastava, and R. S. Sekhon, 1973: Doppler radar characteristics of precipitation at vertical incidence. *Rev. Geophys.*, **11**, 1–35, https://doi.org/10.1029/RG011i001p00001.

Beekhuis, H., and I. Holleman, 2008: From pulse to product: Highlights of the digital-IF upgrade of the Dutch national radar network. *Fifth European Conf. on Radar Meteorology and Hydrology*, Helsinki, Finland, Finnish Meteorological Institute, 120, https://cdn.knmi.nl/system/data_center_publications/files/000/068/061/original/erad2008drup_0120.pdf?1495621011.

Bringi, V. N., and V. Chandrasekar, 2001: *Polarimetric Doppler Weather Radar Principles and Applications*. Cambridge University Press, 636 pp.

——, ——, N. Balakrishman, and D. Zrnić, 1990: An examination of propagation effects in rainfall on radar measurements at microwave frequencies. *J. Atmos. Oceanic Technol.*, **7**, 829–840, https://doi.org/10.1175/1520-0426(1990)007<0829:AEOPEI>2.0.CO;2.

Chen, Y., H. Liu, J. An, U. Gorsdorf, and F. Berger, 2015: A field experiment on the small-scale variability of rainfall based on a network of Micro Rain Radars and rain gauges. *J. Appl. Meteor. Climatol.*, **54**, 243–255, https://doi.org/10.1175/JAMC-D-13-0210.1.

Doviak, R. J., and D. S. Zrnić, 1993: *Doppler Radar and Weather Observations*. Academic Press, 562 pp.

Figueras i Ventura, J., 2009: Design of a high resolution X-band Doppler polarimetric radar. Ph.D. thesis, Delft University of Technology, 182 pp.

Frech, M., M. Hagen, and T. Mammen, 2017: Monitoring the absolute calibration of a polarimetric weather radar. *J. Atmos. Oceanic Technol.*, **34**, 599–615, https://doi.org/10.1175/JTECH-D-16-0076.1.

Giangrande, S. E., and A. V. Ryzhkov, 2005: Calibration of dual-polarization radar in the presence of partial beam blockage. *J. Atmos. Oceanic Technol.*, **22**, 1156–1166, https://doi.org/10.1175/JTECH1766.1.

Gorgucci, E., and L. Baldini, 2015: Influence of beam broadening on the accuracy of radar polarimetric rainfall estimation. *J. Hydrometeor.*, **16**, 1356–1371, https://doi.org/10.1175/JHM-D-14-0084.1.

Gourley, J. J., P. Tabary, and J. P. D. Chatelet, 2006: Data quality of the Meteo-France C-band polarimetric radar. *J. Atmos. Oceanic Technol.*, **23**, 1340–1356, https://doi.org/10.1175/JTECH1912.1.

Holt, A., and J. Shepherd, 1979: Electromagnetic scattering by dielectric spheroids in the forward and backward directions. *J. Phys.*, **12A**, 159–166, https://doi.org/10.1088/0305-4470/12/1/029.

Kowalewsky, S., and G. Peters, 2010: Analysis of *Z–R* relations based on LDR signatures within the melting layer. *J. Atmos. Oceanic Technol.*, **27**, 1555–1561, https://doi.org/10.1175/2010JTECHA1363.1.

Kumar, S., M. Konwar, K. Chakravarty, and S. Deshpande, 2017: Raindrop size distribution of different cloud types over the Western Ghats using simultaneous measurements from Micro-Rain Radar and disdrometer. *Atmos. Res.*, **186**, 72–82, https://doi.org/10.1016/j.atmosres.2016.11.003.

Leijnse, H., and Coauthors, 2010: Precipitation measurement at CESAR, the Netherlands. *J. Hydrometeor.*, **11**, 1322–1329, https://doi.org/10.1175/2010JHM1245.1.

Lengfeld, K., M. Clemens, C. Merker, H. Münster, and F. Ament, 2016: A simple method for attenuation correction in local X-band radar measurements using C-band radar data. *J. Atmos. Oceanic Technol.*, **33**, 2315–2329, https://doi.org/10.1175/JTECH-D-15-0091.1.

——, M. Berenguer, and D. S. Torres, 2018: Intercomparison of attenuation correction algorithms for single-polarized X-band radars. *Atmos. Res.*, **201**, 116–132, https://doi.org/10.1016/j.atmosres.2017.10.020.

Mazari, N., H. O. Sharif, H. Xie, A. E. Tekeli, J. Zeitler, and E. Habib, 2017: Rainfall observations and assessment using vertically pointing radar and X-band radar. *J. Hydroinform.*, **19**, 538–557, https://doi.org/10.2166/hydro.2017.151.

METEK, 2015: MRR physical basics, version 5.2.0.1. Meteorologische Messtechnik GmbH Tech. Rep., 20 pp., https://mpimet.mpg.de/fileadmin/atmosphaere/barbados/Instrumentation/MRR-physical-basics_20090707.pdf

Otto, T., and H. W. J. Russchenberg, 2011: Estimation of specific differential phase and differential backscatter phase from polarimetric weather radar measurements of rain. *IEEE Geosci. Remote Sens. Lett.*, **8**, 988–992, https://doi.org/10.1109/LGRS.2011.2145354.

——, H. W. J. Russchenberg, R. R. Reinoso-Rondinel, C. M. H. Unal, J. Yin, and C. Gatidis, 2010: IDRA weather radar measurements—All data. Processed data with standard range, 4TU.ResearchData, accessed 28 February 2019, https://doi.org/10.4121/uuid:5f3bcaa2-a456-4a66-a67b-1eec928cae6d.

Park, S.-G., M. Maki, K. Iwanami, V. N. Bringi, and V. Chandrasekar, 2005: Correction of radar reflectivity and differential reflectivity for rain attenuation at X band. Part II: Evaluation and application. *J. Atmos. Oceanic Technol.*, **22**, 1633–1655, https://doi.org/10.1175/JTECH1804.1.

Peters, G., B. Fischer, H. Munster, M. Clemens, and A. Wagner, 2005: Profiles of raindrop size distributions as retrieved by Micro Rain Radars. *J. Appl. Meteor.*, **44**, 1930–1949, https://doi.org/10.1175/JAM2316.1.

——, ——, and M. Clemens, 2010: Rain attenuation of radar echoes considering finite-range resolution and using drop size distribution. *J. Atmos. Oceanic Technol.*, **27**, 829–842, https://doi.org/10.1175/2009JTECHA1342.1.

Reinoso-Rondinel, R., C. Unal, and H. Russchenberg, 2018: Adaptive and high-resolution estimation of specific differential phase for polarimetric X-band weather radars. *J. Atmos. Oceanic Technol.*, **35**, 555–573, https://doi.org/10.1175/JTECH-D-17-0105.1.

Richter, C., and M. Hagen, 1997: Drop-size distributions of raindrops by polarization radar and simultaneous measurements with disdrometer, windprofiler and PMS probes. *Quart. J. Roy. Meteor. Soc.*, **123**, 2277–2296, https://doi.org/10.1002/qj.49712354407.

Rinehart, R. E., 2004: *Radar for Meteorologists*. Rinehart Publishing, 464 pp.

Ryzhkov, A., and D. Zrnić, 2005: Radar polarimetry at S, C, and X bands: Comparative analysis and operational implications. *32nd Conf. on Radar Meteorology*, Albuquerque, NM, Amer. Meteor. Soc., 9R.3, https://ams.confex.com/ams/32Rad11Meso/webprogram/Paper95684.html.

Scarchilli, G., E. Gorgucci, V. Chandrasekar, and A. Dobaie, 1996: Self-consistency of polarization diversity measurement of rainfall. *IEEE Trans. Geosci. Remote Sens.*, **34**, 22–26, https://doi.org/10.1109/36.481887.

Sekhon, R. S., and R. C. Srivastava, 1971: Doppler radar observations of drop-size distributions in a thunderstorm. *J. Atmos.*

Sci., **28**, 983–994, https://doi.org/10.1175/1520-0469(1971)028<0983:DROODS>2.0.CO;2.

Testud, J., E. L. Bouar, E. Obligis, and M. Ali-Mehenni, 2000: The rain profiling algorithm applied to polarimetric weather radar. *J. Atmos. Oceanic Technol.*, **17**, 332–356, https://doi.org/10.1175/1520-0426(2000)017<0332:TRPAAT>2.0.CO;2.

Tridon, F., J. V. Baelen, and Y. Pointing, 2011: Aliasing in Micro Rain Radar data due to strong vertical winds. *Geophys. Res. Lett.*, **38**, L02804, https://doi.org/10.1029/2010GL046018.

Unal, C., 2009: Spectral polarimetric radar clutter suppression to enhance atmospheric echoes. *J. Atmos. Oceanic Technol.*, **26**, 1781–1797, https://doi.org/10.1175/2009JTECHA1170.1.

van Baelen, J., Y. Pointin, W. Wobrock, A. Flossmann, G. Peters, F. Tridon, and C. Planche, 2009: Precipitation and microphysical studies with a low cost high resolution X-band radar: An innovative project prospective. *Adv. Geosci.*, **20**, 25–32, https://doi.org/10.5194/adgeo-20-25-2009.

Vulpiani, G., M. Montopoli, L. D. Passeri, A. G. Gioia, P. Giordano, and F. S. Marzano, 2012: On the use of dual-polarized C-band radar for operational rainfall retrieval in mountainous areas. *J. Appl. Meteor. Climatol.*, **51**, 405–425, https://doi.org/10.1175/JAMC-D-10-05024.1.

Wingo, S. M., W. A. Petersen, P. N. Gatlin, C. S. Pabla, D. A. Marks, and D. B. Wolff, 2018: The System for Integrating Multiplatform Data to Build the Atmospheric Column (SIMBA) precipitation observation fusion framework. *J. Atmos. Oceanic Technol.*, **35**, 1353–1374, https://doi.org/10.1175/JTECH-D-17-0187.1.

Yin, J., C. Unal, and H. Russchenberg, 2019: Object-orientated filter design in spectral domain for polarimetric weather radar. *IEEE Trans. Geosci. Remote Sens.*, **57**, 2725–2740, https://doi.org/10.1109/TGRS.2018.2876632.

Zrnić, D. S., and A. Ryzhkov, 1999: Polarimetry for weather surveillance radars. *Bull. Amer. Meteor. Soc.*, **80**, 389–406, https://doi.org/10.1175/1520-0477(1999)080<0389:PFWSR>2.0.CO;2.